Damiano Zito
Progold S.p.A.

Damiano Zito is the CEO of Progold S.p.A. which produces precious and semi-finished metal alloys in gold, platinum and titanium obtained directly with 3D printing.
He is a member of the Board of Federorafi and is assigned to Regulations and Innovation, is Chairman of the "Gems and precious Metals Group" of the Italian Unification Body (UNI) and chairman of the entrepreneurial area Advisory Board of the "CUOA Foundation" Business School of Altavilla Vicentina.
For his thirty years experience in the sector and prolific research activities, in 2006 he was assigned the title of ambassador of the Santa Fe' Symposium, of which he was a speaker in 6 editions. His company's Research and Development Department has received best research awards 6 times.

Direct metal printing changes the rules when creating innovative jewels. Selective laser melting (SLM™) enables researchers to become creative and use new materials. This research tests different, new products, exploring new SLM horizons using incredible materials for gold-working applications.

Additional manufacturing through selective laser melting creates the opportunity to combine materials with thoroughly different properties, in ways that would be impossible otherwise. What incredible new possibilities can we expect while learning from the surprising properties obtained?

“3D direct metal printing: a trip through new opportunities and innovative alloys”

Damiano Zito
Progold S.p.A.

INTRODUCTION

The brief historical journey travelled so far with selective laser melting (SLM™) has led us to managing this manufacturing process with more self-confidence and versatility; starting from the first selection experiments on basic parameters and the choice of alloys [1, 2, 3] up to the latest challenges between the performance of investment casting and that of selective laser melting to create complex decorative elements [4] and lastly the real production needs of jewellers. These promising results have led us to see that selective laser melting can be used to produce potentially interesting innovative materials when manufacturing jewels.
The current panorama in the gold sector is undoubtedly focussed on materials with surprising aesthetic and mechanical characteristics. During this study, we have described some experiments on the production of metallic glass and metallic matrix composites through selective laser melting (SLM™). Metallic glass is a recent development in the metal-working of precious stones [5, 6] and provides extremely hard alloys with really low processing temperatures. However, production of these metals through classic investment casting has limits when manufacturing thick items; because of the high thermal inertia meaning that the amorphous stage cannot be maintained. The selective laser melting technique could get round this thermo-dynamic problem thanks to the high cooling kinetics guaranteed by the points melting of material.
Metallic composites, obtained by adding refractory powdered metals, can display new mechanical and colour gradients because of the particular extraneous stages introduced to create the alloys in various golden shades, including the high concentration ones. The selective laser melting technique could be an alternative way to produce alloys with refractory metals; elements that are extremely difficult to bind with gold because of their high melting temperature, their tendency to create a high quantity of waste and the high reactivity with the crucibles commonly used in melting [7].

EXPERIMENTAL PROCEDURE

The precious alloys were pulverised in a gas atomiser, protected through an inert argon atmosphere, thus creating a dry, uniform mass of spherical particles. These conditions are really important for getting the powder to slide well under the brushes that spread it on the construction platform. The experimental articles were printed using the same selective laser melting machine as the previous research (ReaLizer SLM50), equipped with a 100 W fibre laser, collimated in a 10 µm ray.
The shape of the powder particles was observed through a scanning electron microscope (SEM) and the particles were distributed by a laser granulometre (Malvern, Hydro 2000S). The particles were effectively distributed removing the larger ones with a 53 µm squared mesh stainless steel sieve. The raw materials to synthesise the metallic glass were pre-bound in an open caster at 700°C, under the protection of argon and poured into a cold cast iron mould to obtain a homogeneous ingot to be atomised. The composition of the alloy (1) to laser print the metallic glass was chosen from amongst those frequently mentioned in literature and patents [5] containing palladium, copper, silver and silicon bound with gold (Table 1). The structural presence of the alloy’s non crystalline stage was calculated through a scale for differential thermal analysis (DTA) in aluminium crucibles (Seiko, Exstar 6300) and through x-ray scattering techniques (XRD, Philips PW3710/1830, geometry Bragg-Brentano). On the other side, the raw materials for the synthesis of the composites in precious matrix except for refractory metal were bound through abrasive blasting in water and then pulverised in the atomiser (Table 1). The refractory metal in powder form was added later and homogenised to the preceding part with a planetary mixer (Glenn Mills, Turbula T2F), obtaining a uniform mixture ready for the laser melting process.
The typical procedure to create a real jewellery item, for example a wedding ring in glassy alloy, basically consists in selecting the best laser parameters, as was shown in the first works [1, 2, 3, 4].

ALLOY	Au	Ag	Pd-Ni	Cu	Si	Nb	Zn	Ti
1	76.26	4.69	1.93	13.5	3.62	0.00	0.00	0.00
2	75.20	0.00	0.00	0.00	0.00	18.5	6.30	0.00
3	75.20	8.40	0.00	0.00	0.00	0.00	0.00	16.4

Table 1 Overall composition of alloys (%p) for the selective laser melting.

The model used for this primary parameter selection was the classic lamellar solid formed by vectors produced from a single laser scan (Figure 1). The lamellar model is an extremely useful tool to check regular melting of the laser line and detect dangerous porosities and anomalies when the vectors are solidifying. In other words, the solidity and regularity of the single vector in these ideal tests are the first essential conditions for obtaining solid, reliable items in jewellery. Moreover, stamping single vectors also enables us to detect their length; fundamental for a first setting of the distance between vectors when constructing solid pieces.

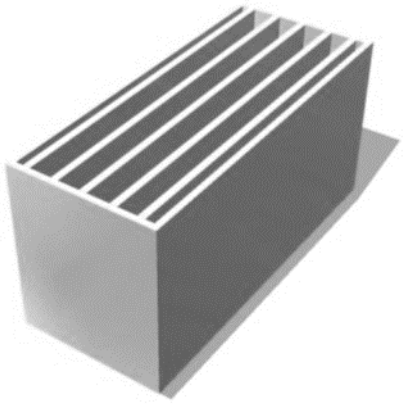

Figure 1 Lamellar sample ideal to control vector quality.

On the other hand, construction of the solid models (Figure 2) was used to perfect the melting strategy, including the distance of vectors, called hatch distance and the laser scanning method. During research, two solid model types were chosen, based on the work stage they were intended for. The first solid model is a small rectangular prism (10.0´4.5´3.0 mm) used in the first research stage, enabling construction of a high number of pieces on a single platform, thus accelerate selection of the best print parameters.

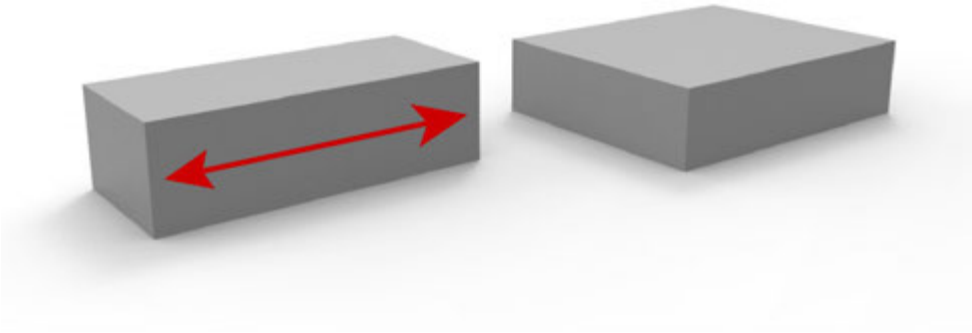

Figure 2 Layout of solid samples and roughness measurement direction.

Moreover, the elongated shape of this model enables the highlighting of any alloy tendency to withdraw in size, usually shown by the ends of the piece lifting up and supports coming off (Figure 3).

Figure 3 Example of samples with the ends rising and supports coming off.

Once the most promising laser parameter combinations have been identified, the second, larger solid model (10.0´8.0´2.5 mm) was used in the second part of the experiment to determine alloy colour. The roughness of items printed was measured by a profilemetre (Taylor Hobson®, Form Talysurf Intra2) equipped with a 2.0 µm diamond-tipped probe. Roughness measurements were taken horizontally along the two longer faces of the solid models (Figure 2). Hardness was measured on the larger prisms using a Vickers durometer (Future-Tech, Microhardness tester FM), with measurement uncertainty of around ±15 HV. While the colour was determined thanks to a digital colourmeter (Gretag MacBeth, Color i5).
The number and direction of the laser passages define the scanning method of the stretch along the plane and between each construction layer and the next. This research examined five different laser scanning types. The first scanning method was from the simple overlapping of the laser scans vertically (Figure 4), indicated by the symbol X, by which the laser ray always scans the same position along all the construction layers. The second type foresees a laser scan in the middle of the vectors of the previous layer, indicated with X½. The third foresees a double scan within the same layer, with the second passage in the middle of the vectors of the first passage, indicated by XX (Figure 5). The fourth type foresees perpendicular rotation of the laser scan with respect to the scanning direction of the previous layer and is indicated by XY (Figure 5); while the fifth and last scanning type is created with three consecutive laser passages over the same construction layer, two of which on the same position and the last in the middle of the previous ones, indicated by the symbol XXX (Figure 6).
Continual rotation of scans could ensure a significant reduction in the thermal tensions and geometrical deforming of models (Figure 7), while the multiple scans generally ensure less porosity of the pieces. Once the series of models planned by the experimental plan had been made, the best constructive parameter combination in terms of greater density and hardness of pieces was used to print some real jewellery pieces.
The jewellery items chosen are a hollow ring for the glassy alloy and a full ring for the composite alloys (Figure 8). Figure 9 shows the general flow diagram of the operations performed in this research, in which each selection process is followed by a quality control of pieces printed to obtain, by exclusion, the most suitable series of laser parameters to produce real gold items.

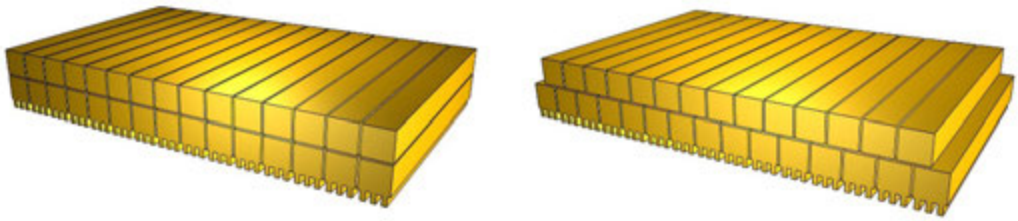

Figure 4 Scanning method with vectors stacked X (left) and moved in the middle X½ (right).

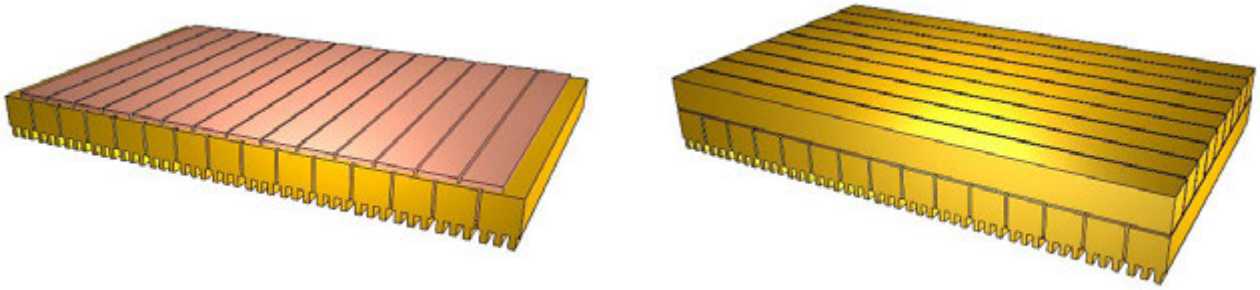

Figure 5 Scanning method with central passage XX (left) and normal rotation of the scans XY (right).

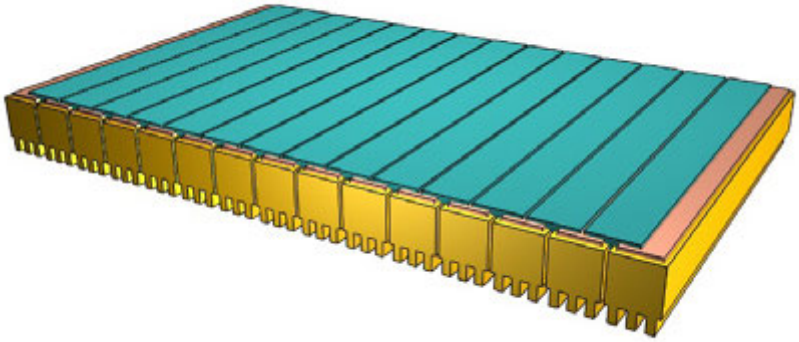

Figure 6 Scanning method with triple laser passage XXX on each construction layer.

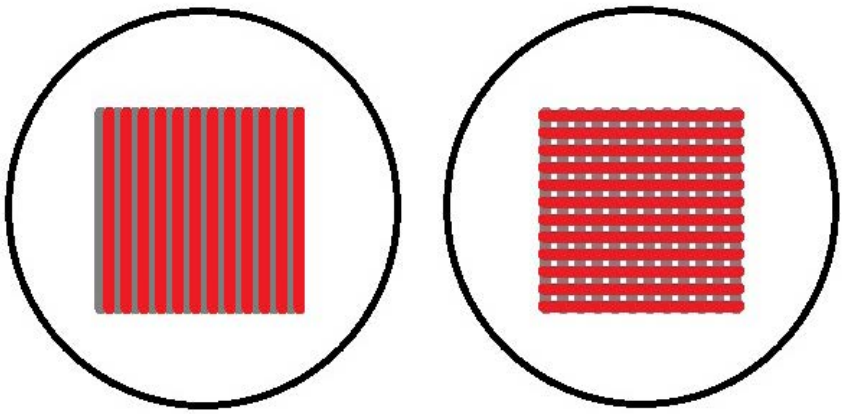

Figure 7 Upper view of the scan moved into the middle XX (left) and of the rotated one XY (right).

Figure 8 Diagram of the engagement and wedding ring models.

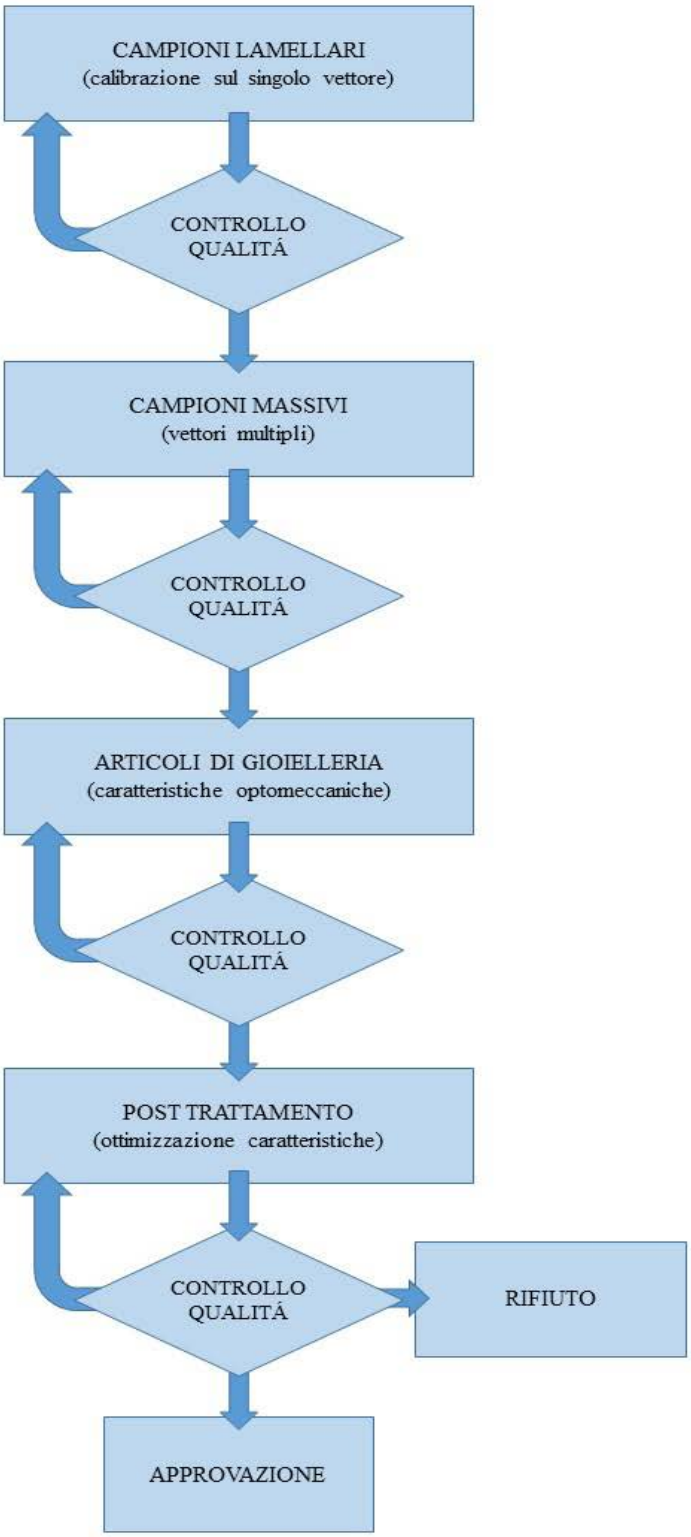

Figure 9 Diagram of the general research flow.

EXPERIMENTAL RESULTS AND DISCUSSION

Amorphous alloy

Atomising the composition of the metallic glass led to formation of the typical distribution of spherical particles arising from the gassy pulverisation of the melted alloy, together with the presence of sporadic elongated particles (Figures 10, 11), probably due to the not perfectly correct ratio between atomising temperature (600°C) and the remarkable viscosity of the melted alloy (1) caused by the high silicon content. The particles representing half the volume of powder (D50) are smaller than 24 µm, while ninety percent of the powder volume is formed by particles with a diameter of less than 51 µm (D90).
The differential thermal analysis (DTA) confirmed the persistence of the metallic glass in the powder just atomised (Figure 12). The exothermic peak at about 180°C represents the crystallisation process of the amorphous stage and the endothermic peak around 350°C indicates the liquidus temperature of the alloy (1). Moreover, the alloy's glassy transition temperature (Tg), identifiable from the signal's change in pitch, takes place around 130°C and enables the material to be easily deformed. The ratio between the area of the first crystallisation peak and the area of the melting peak, which we will call disorder factor (ef), is correlated with the reticular disorder and with the glassy fraction of the alloy after atomisation: the higher its value the greater the fraction of the amorphous stage. In the glassy alloy powder just atomised ef is approximately 0.63, a value that bibliographic sources [8] show belong to an alloy that is just about completely amorphous. The uncertainty of measurement on this disorder is about 10%, based on tests repeated on the same sample.

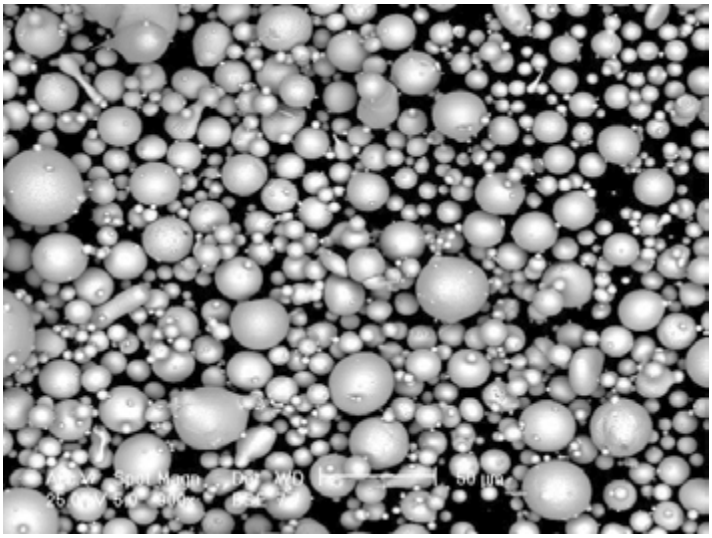

Figure 10 Scanning electron microscopy of the powders of Au76.26Ag4.69Pd1.93Cu13.5Si3.62.

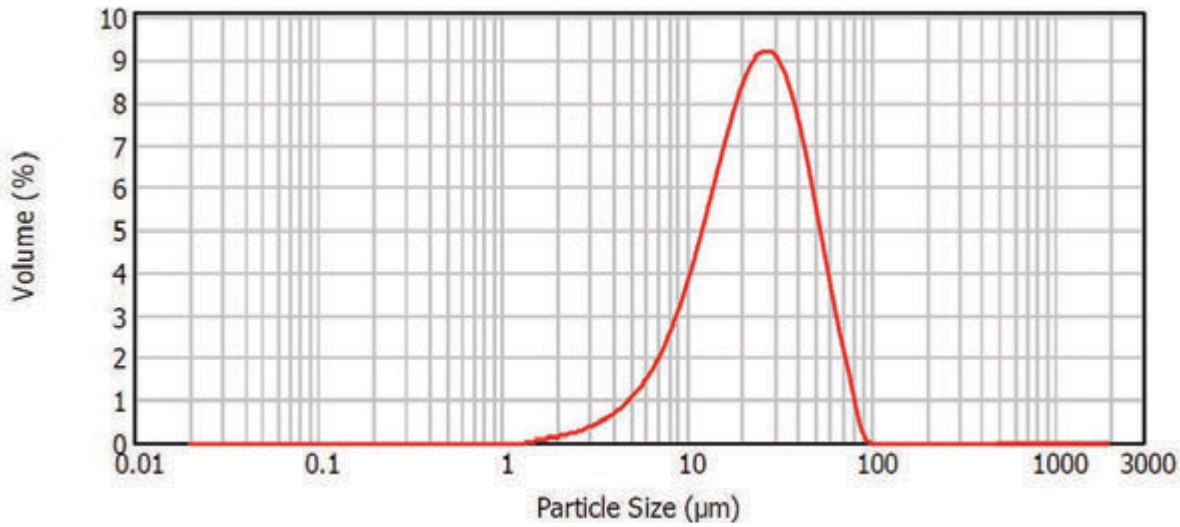

Figure 11 Size distribution of the particles in the glassy alloy Au76.26Ag4.69Pd1.93Cu13.5Si3.62.

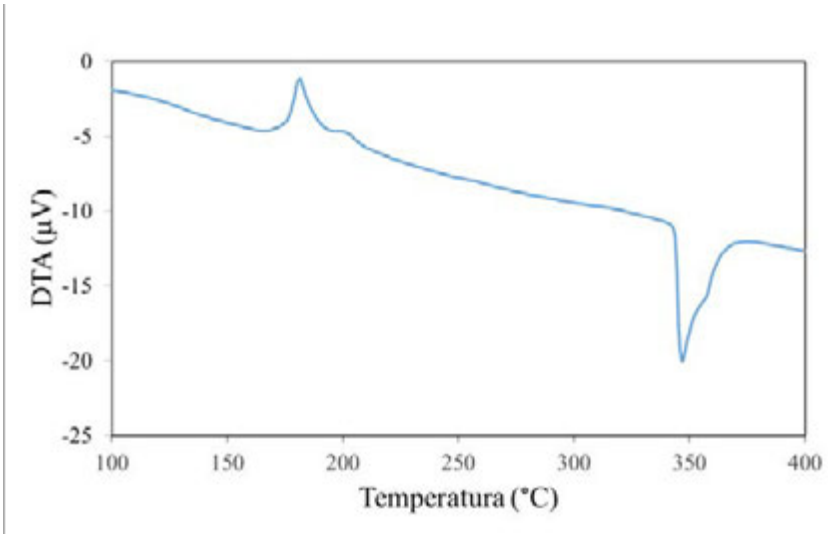

Figure 12 Differential thermal analysis of the powder of glassy alloy Au76.26Ag4.69Pd1.93Cu13.5Si3.62.

The initial tests were performed with a scan speed of 0.25 m/s, while laser power was varied between 50 and 20 W (Figure 13). Pieces acceptable in aspect and completeness were built with a laser power of between 37.5 and 50 W. The laser power and the approximate completion percentage of the lamellar pieces obtained by the best platform can be found in Table 2.

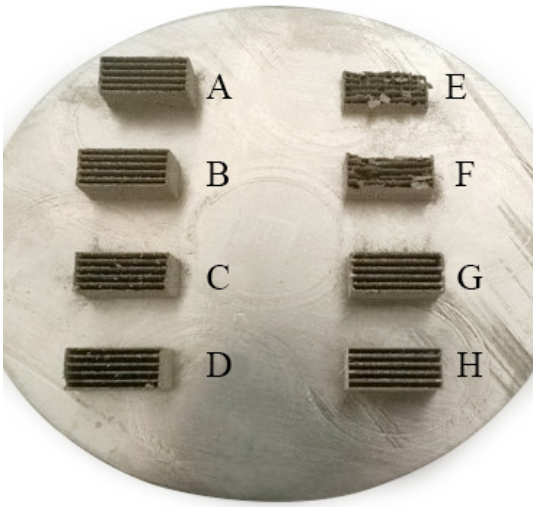

Figure 13 Lamellar vectors based on laser power.

SAMPLE	LASER POWER (W)	COMPLETION (%)
A	37.5	100
B	37.5	100
C	25.0	90
D	25.0	90
E	20.0	20
F	20.0	20
G	50.0	100
H	50.0	100

Table 2 Laser parameters and completion level of pieces based on laser power.

In order to maintain a significant fraction of glassy stage in the alloy and a maximum level completion percentage, the scanning speed was gradually increased from 0.25 to 5 m/s. These attempts were suggested by a a lower energy transfer that could be given to the metallic glass particles and by the resulting reduction in general overheating responsible for the greater crystallisation phenomenon.
The overall results indicated that, for a laser power of 50 W, completion of lamellar vectors is always maximum (100%); while for powers of 37.5 W, completion of pieces is only found for speeds of or less than 0.5 m/s. On the other hand, the disorder factor decreases as the laser irradiation duration increases, as indicated by the differential thermic analysis through the progressive relative reduction of the frst crystallisation peak area (Figure 14). With a laser power of 50 W, the disorder factor reduction and corresponding irradiation duration are indicated in Table 3.

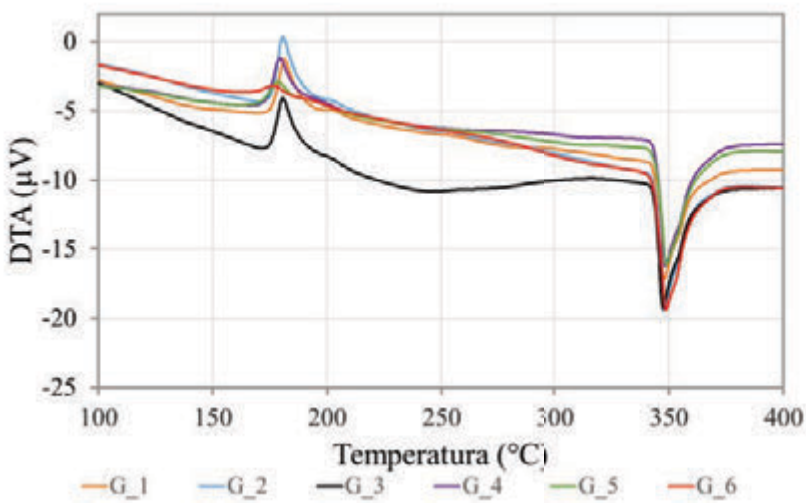

Figure 14 Reduction of the crystallisation peak based on exposure time.

SAMPLE	SCANNING SPEED (m/s)	ef
G_1	5	0.52
G_2	2.5	0.57
G_3	1	0.54
G_4	0.5	0.45
G_5	0.33	0.39
G_6	0.25	0.14

Table 3 Disorder factor based on scanning speed.

However, conserving a disorder factor for the glassy stage near to the one of the atomised powder and maximum geometrical completion of the lamellar models does not, in any case, guarantee adequate solidity and regularity of vectors printed. The metallographic sector revealed the typical imperfections of vectors not perfectly solidified, that is with undulated profiles and interruptions (Figure 15).

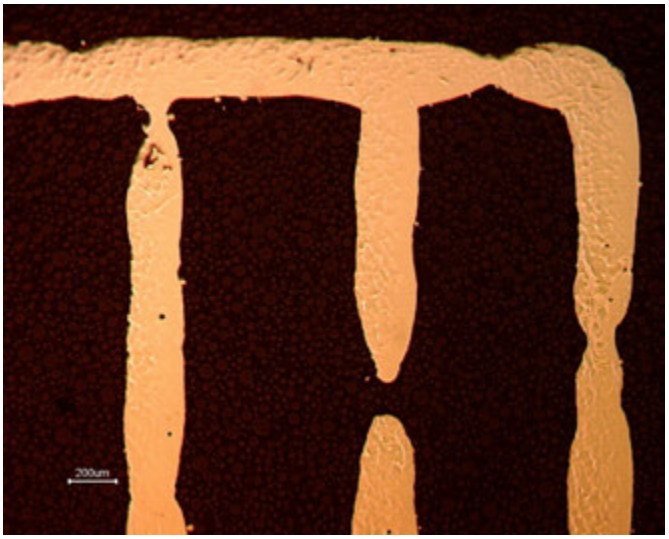

Figure 15 Typical vector anomalies with laser power of 50 W.

The best condition for avoiding vector anomalies and maintain an adequate glassy stage fraction was found by increasing laser power to 62.5 W with a scanning speed of 1 m/s as shown in Table 4. This table also lists the samples with identical scanning speed, due, however, to different constituting parameter combinations. The significant persistence of the glassy stage was detected measuring a fairly strong crystallisation signal in differential thermal analysis (Figure 16) and the regularity of single vectors was confirmed by the metallographic section of the respective lamellar piece (Figure 17).

SAMPLE	LASER POWER (W)	SCANNING SPEED (m/s)	ef
L_1	62.5	5	0.54
L_2	62.5	3.3	0.59
L_3	62.5	1.6	0.47
L_4	62.5	2.5	0.53
L_5	62.5	1.6	0.51

Table 4 Print parameters and disorder factor for a laser power of 62.5 W.

Having achieved vector regularity, the constructions parameters, i.e. laser power 62.5 W and a speed of 1 m/s, were used as starting parameters for the production of solid models (Figure 2), shaped like a rectangular prism (10.0´4.5´3.0 mm).

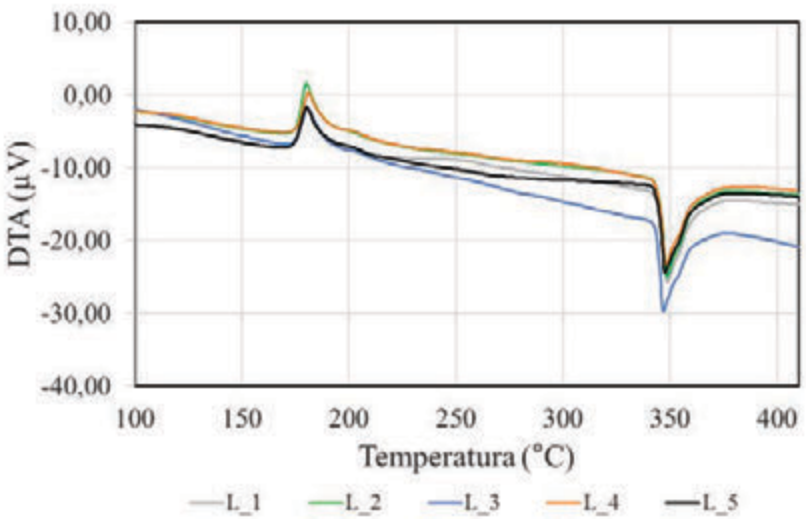

Figure 16 Differential thermal analysis of printed samples with laser power of 62.5 W.

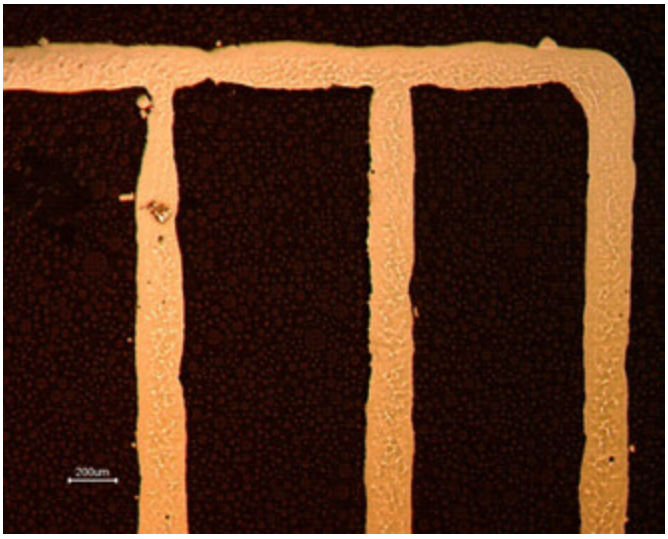

Figure 17 Typical aspect of uniform lamellar vectors of sample 3 (Table 4).

The construction tests of solid prisms executed scanning vectors moving continuously in the middle of previous layers or in the middle of the same construction layer (X½, XX) led to better results in general porosity terms (Tables 5 and 6). Similarly the reduction of the hatch distance tends to reduce material porosity. However, when this distance drops around 130 µm, fragile fractures start to appear, causing the piece to break up spontaneously, probably because of the strong tensions caused by the considerable crystallisation of the material. solid samples built with the four parameter types considered the best were analysed through DTA and XRD to calculate the glassy fraction. The variations in the disorder factor values, calculated through DTA technique agree with the difference in the amorphous stage percentage estimated by x-ray scattering, considering the experimental uncertainty (±10 % DTA, ±5% XRD) and the great difference in sample quality analysed with the two techniques, equal to 20 mg for the differential thermal analysis and 2000 mg for the x-ray scattering, equivalent in this latter case to the entire sample. This difference in masses analysed can explain the greater crystallinity detected by the thermal analysis for the samples (D) compared to values measured by scattering: the difference observed is probably due to sample inhomogeneity. Both techniques reveal good persistence of the amorphous stage in samples printed, except in the case of the last combination of parameters (D), where you can note a significant increase in crystallinity.(Table 6).

ALLOY	SAMPLE	LASER POWER w	SCANNING SPEED (m/s)	DISTANCE VECTORS (µm)	SCANNING
1	A	62.5	1	200	X½
	B	62.5	3.3	200	X½
	C	62.5	3.3	200	XX
	D	62.5	3.3	180	XX

Tabella 5 Best laser parameter combinations for selective laser melting of the glassy alloy.

ALLOY	SAMPLE	L*	a*	b*	Y.I.	Rtot (µm)	HARDNESS (TBC)	ef	AMORPHOUS STAGE (% p)
1	A	83.27	1.25	8.45	18.51	69	415	0.48	85.1
	B	81.38	1.04	7.75	17.27	48	401	0.55	83.2
	C	70.04	2.32	10.00	25.70	76	381	0.50	91.2
	D	80.52	0.94	7.85	17.51	39	441	0.21	70.6

Table 6 Optomechanical characteristics of the glassy alloy in function of laser parameters.

Amongst jewels printed, hollow rings similar to an engagement ring (Figure 8), the sample printed with laser power of 62.5 W, a scanning speed of 3.3 m/s, hatch distance at 200 µm and using an X½ scanning method (B), revealed greater persistence in the amorphous stage. In this case the DTA analysis shows a high disorder factor value (ef = 0.54±0.05, Figure 19), confirmed by the x-ray scattering, indicating a high percenatge in amorphous stage weight (92±5%, Figure 20).
The aesthetic aspect of this ring displays good shape consistency compared to the digital model; even though there is evidence of significant general roughness (Figure 18) and porosity is still considerable, but less than what was found with other parameters. Unfortunately, the most serious problems when manufacturing this type of glass alloy lie in the finishing process and colour stability. It was generally noted that the grinding and polishing processes can easily lead to localised deformation; due to overheating under the process brushes and the low material softening point. In this case, a finishing system that maintains the piece at a relatively low temperature, such as tumbling and electro-cleaning, could be preferable.

Figure 18 Hollow ring after laser printing.

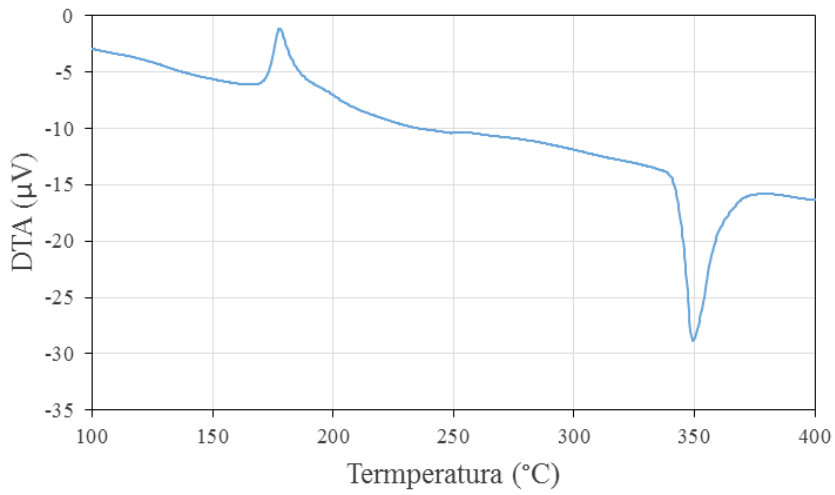

Figure 19 Differential thermal analysis of the ring produced with (B) parameters

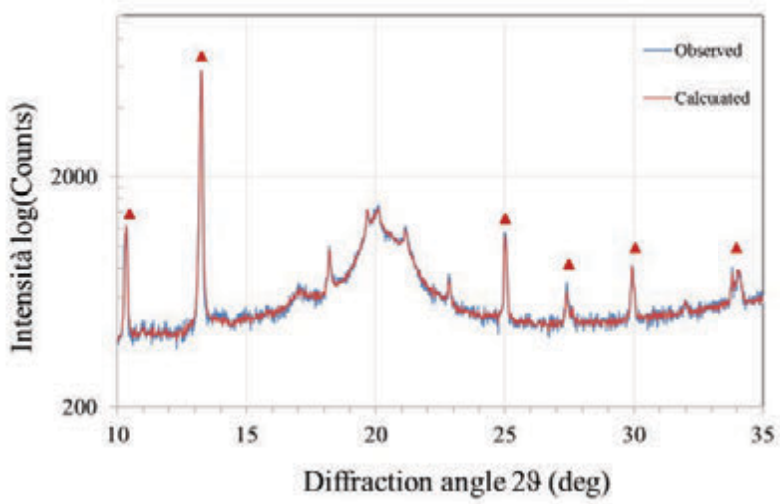

Figure 20 X-ray scattering of the ring (B). Internal standard peaks indicated with a triangle.

The glassy alloy was also examined in colour stability terms as, in general, this type of material suffers from a very low resistance to oxidation. The resistance to oxidation test was conducted in artificial sweat created by sodium chloride, urea and lactic acide for seven days based on the standard procedure (UNI EN 1811:2015); to appreciate any optic alterations. The colour difference between the ring just polished and the one exposed to synthetic sweat was considerable (Figures 21 and 22).

Figure 21 Hollow ring in glassy alloy after polishing.

Figure 22 Hollow ring in glassy alloy after the artificial sweat test.

COMPOSITE ALLOYS

Selective laser melting was then used to synthesise gold alloys with refractory metals. This metals family has a high melting point and considerable resistance to wear and the current extended definition includes fourteen elements (Ti, V, Cr, Zr, Nb, Mo, Ru, Rh, Hf, Ta, W, Re, Os, Ir); each of which with serious difficulties for use in goldsmithery because of their low solubility in gold and high reactivity with oxygen, nitrogen and the melting crucible. For example, niobium and titanium are generally used as hardening and strengthening additives in structural alloys, such as stainless steel and aerospace alloys. Their solubility in the precious matrices is limited in normal conditions. However, these metals have a considerable whitening and hardening power, something that makes them highly desirable in jewellery (Figures 23, 24).
To get over these problems and preserve the beneficial performance of these two elements, a series of selective laser meltings were performed for each refractory metal on mixtures of the two different powder types. The first powder type was obtained by binding the gold with an auxiliary metal (Ag, Zn) through atomisation and constitutes the precious matrix of the end mixture; while the second type is formed by the pure refractory element. A specific ratio of two powder types is then suitably mixed in a planetary homogeniser, to obtain the final alloy compositions (Table 1).

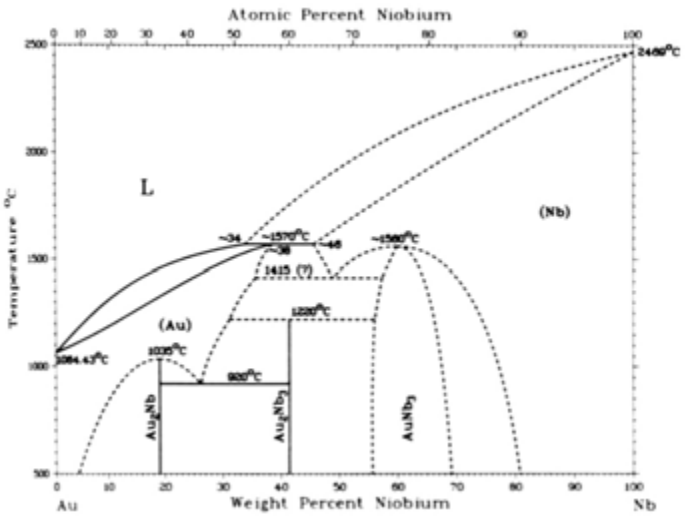

Figure 23 Binary stage diagram for the gold niobium system.

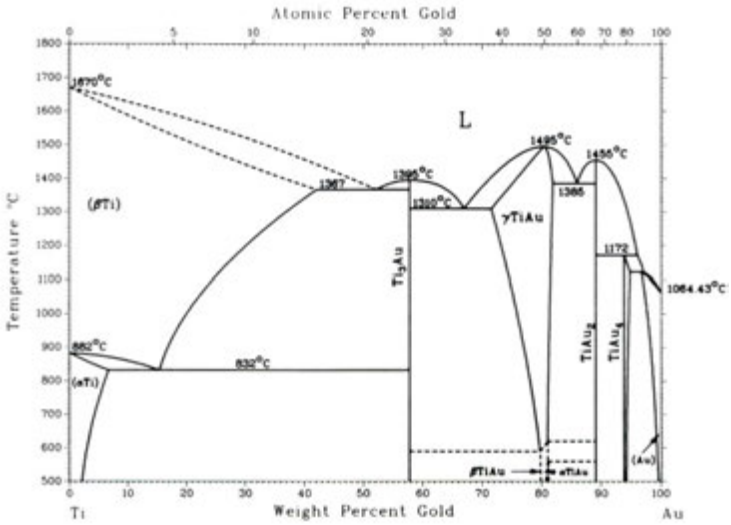

Figure 24 Binary stage diagram for the gold titanium system.

The function of the auxiliary metal is to limit addition of refractory metal which could be an obstacle to melting or form critical quantities of fragile intermetallic alloys and to regulate the legal concentration of the material printed. While the function of the precious matrix is to uniformly disperse the refractory metal and enable as greater quantity of solubilisation as possible.
The first composite alloy (2) analysed is based on a precious matrix formed by 932.5%p in gold and 7.5%p in zinc (Figure 25), with the addition of niobium powder so that it had respectively the final standard 18.5%p. The zinc used in alloy as an auxiliary metal could invalidate the production quality in the selective laser melting technique; but, thanks to its low melting (420°C) and boiling (907°C) points, could bring unexpected benefits, once the laser power has been calibrated. The composition of this alloy did not cause any particular atomisation problems. In fact, the powder morphology (Figure 25) and size distribution of the particles (Figure 26) obtained comply with standard process characteristics, with a D50 equal to 19.3 µm and a D90 to 40.3 µm. The morphology or the powder mixture of the precious matrix shows good homogenisation of the refractory metal and accetable size comparability; even though the niobium particles used for this preliminary research are polygonal instead of spherical (Figure 27). In general, we know that spherical particles are better for selective laser melting. However, polygon particles were used for this introductory work as they are easier to find on the market. However, the presence of non spheric particles had no repercussions on the mixture's fluidity, for both the tests of Carney (ASTM B417-89) and Hall (ASTM B213-03), with values of respectively 2.3 s and 8.8 s for the fall of a 50 g powder mass. Further analyses with spheric niobium particles are in progress to assess the impact of refractory morphology on the printing results.

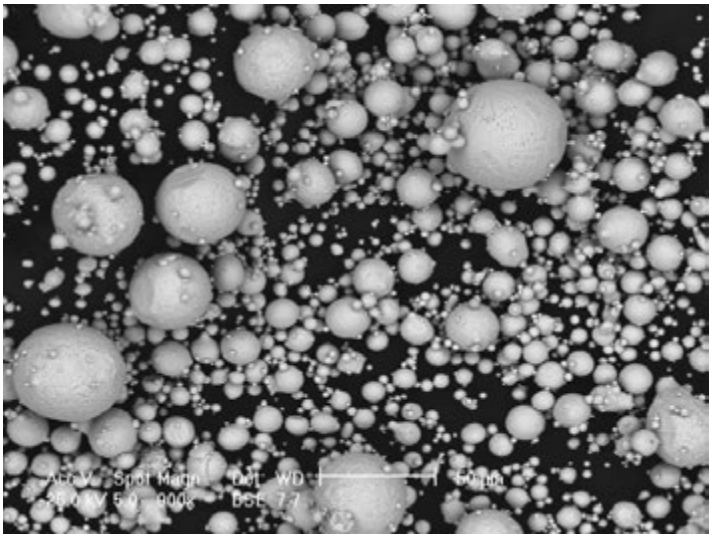

Figure 25 Scanning electron microscopy of the gold zinc matrix.

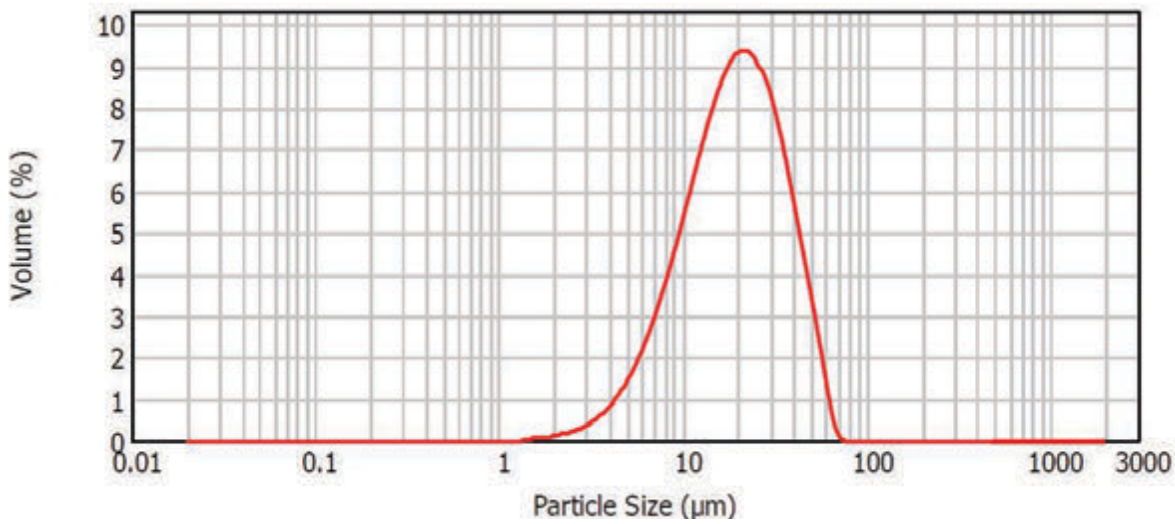

Figure 26 Granulometric distribution of gold zinc matrix.

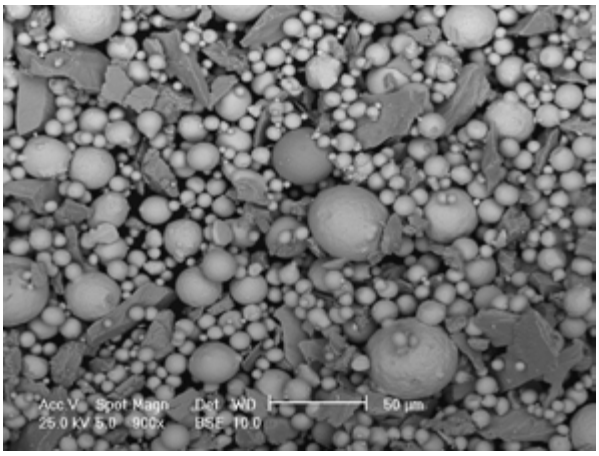

Figure 27 Scanning electron microscopy of the mixture of powders for the alloy (2).

Similarly to the glassy alloy, the best printing parameter combinations were chosen starting from the lamellar and solid models. The four laser parameter combinations and the properties of the relative samples are listed in tables 7 and 8.

ALLOY	SAMPLE	LASER POWER (W)	SCANNING SPEED (m/s)	DISTANCE VECTORS (µm)	SCANNING
2	A	37.50	0.25	130	XY
	B	37.50	0.25	150	XY
	C	37.50	0.33	130	XY
	D	43.75	0.33	150	XY

Table 7 Best laser parameter combinations for the selective melting of Au-Zn-Nb 750‰ (2).

ALLOY	SAMPLE	L*	a*	b*	Y.I.	Rtot (µm)	HARDNESS (HV)
2	A	77.92	1.39	11.15	24.94	62	266
	B	80.43	1.73	11.69	24.38	63	292
	C	72.62	1.64	11.85	27.99	58	272
	D	76.32	1.31	10.04	23.08	59	274

Table 8 Optomechanical characteristics in function of laser parameters for the alloy (2).

In the case of composite materials with niobium, the general characteristics of the items printed show a precious matrix constituted by a solid solution of gold and zinc hosting niobium particles.
These polygonal niobium particles (Figure 28) are very probably due to its incomplete solubilisation in samples just printed; in turn linked to the intrinsic speed of the selective laser melting process, which does not give the entire refractory mass of niobium enough time to dissolve. On the other hand, the relatively pure argon atmosphere (<0.1% O2) and speed of the local melting process help avoid the niobium from oxidising.
The map of elements has showed that the distribution of single metals in the alloy (Figure 29), revealing the presence of niobium in the precious matrix as well as more or less pure niobium particles, confirming at least a partial solubilisation of the refractory metal.

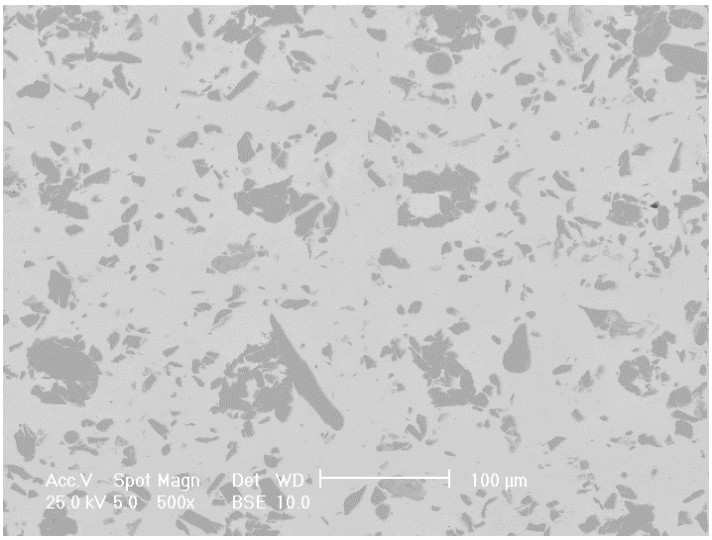

Figure 28 Scanning electron microscopy of the alloy (2) after the laser printing (B).

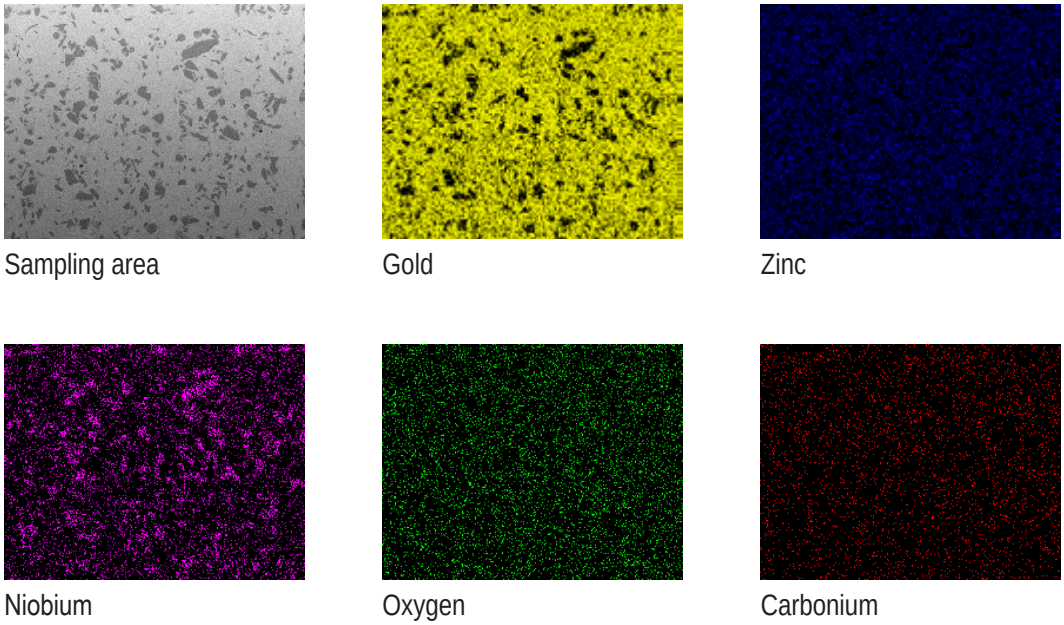

Figure 29 Map of the elements for the alloy (2) after laser printing.

These particles of niobium (10–50 µm) structurally strengthen the gold zinc matrix, though they do not permit real solution of the solid state. The precious matrix soaks the niobium particles adhering solidly and continuously. At an optic level, the presence of these uniformly distributed niobium particles can alter the gleam on the end jewels. The relative disadvantage of the optical disturbance due to the presence of the niobium particles could be reduced further promoting the atomic spread of the niobium in the precious matrix.
The gold concentration was analysed on the printed items, to investigate accuracy and the homogeneousness of the gold content. These analyses, performed with fluorescent x-ray techniques (Bruker Tiger 8, Thermo Scientific Niton XL2 800P) and cupellation (UNI EN ISO 11426:2000), have revealed a considerable non uniformity of the gold concentration, with it varying between about 70% and 78%. This wide variability could be due to use of non-spheric particles of niobium which could have somehow favoured a non homogeneous distribution of the mixture elements on the print table. Moreover, the different granulometric distribution

amplitude of powders used could have played an important role in this result, given the tendency of the smaller fraction particles, only found in the precious matrix, to sediment during the printing process. To solve this problem, alongside the tests planned with spherical niobium particles, future studies will also be oriented towards using particles with granulometry purified of the smaller fraction and of the same distribution in size between precious matrix and refractory metal.
A better spread of the undissolved particle niobium was attempted through solubilising treatments. The first attempt to solubilise the niobium particles was performed from a temperature (680°C) (Figure 30), but the treatment was not sufficient to spread the refractory metal fully.

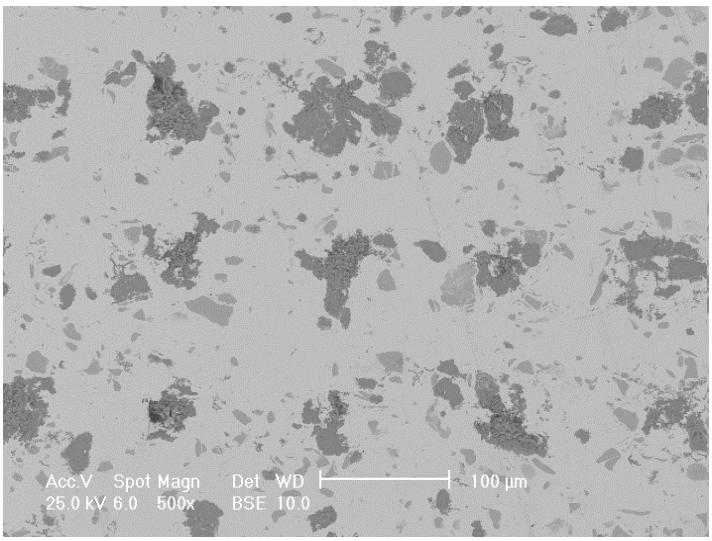

Figure 30 Scanning electron microscopy of the alloy (2) after being solubilised at 680°C for 30 minutes (N_2/H_2).

Solubilisation at higher temperatures (750°C, 800°C) led to a considerable reduction in the particles of pure niobium initially included in the articles just printed (Figures 31, 32); probably due to the refractory metal being absorbed by the precious matrix. Morover, at a temperature of 750°C there is an increase in the material's internal porosity, due to the residual cavities left by the disappearance of the pure niobium particles. At a temperature of 800°C this tendency is decidedly less, probably due to greater material densification. In turn, porosity is responsible for the reduction in hardness observed in samples solubilised at 750°C compared to values obtained with the solubilisation treatment at a lower temperature (Table 8). In the case of the sample treated at 750 °C in N2/H2 we also noted an important variation in the yellow index; this could be due to a partial reaction of the niobium with the nitrogen in the chamber. In addition, given the high percentage of niobium, even small quantities of oxygen present during the solubilisation process can lead to large quantities of niobium oxide forming, already visible with the electronic microscope as a dark mass with treatment at 680°C (Figure 30). These particles can contribute to increasing sample hardness, but prove to be a problem for the subsequent polishing of pieces. Therefore, treatments at 750°C and 800°C in argon were performed in a closed system and in protected atmosphere with repeated washes of the inert gases; they had better results from this point of view, with a much lower oxide incidence (Figures 31, 32). The considerable solubilisation of the niobium at 750°C provides a yellow indicator equal to 17.08, corresponding to a premium white colour, while increasing the piece's hardness to 319 HV (Table 9). With treatment at 800°C the solubilization obtained was just about complete, as the map also confirms (Figure 33). However, hardness and yellow indicator are worsened slightly, probably because of the reduced quantity of intermetallic composites in the materials caused by the higher temperature.

TEMPERATURE:	GAS	L*	a*	b*	Y.I. (D1925)	HARDNESS (HV)
after printing (A)	Ar	77.92	1.39	11.15	24.94	266
after printing (B)	Ar	80.43	1.73	11.69	24.38	292
680°C 30 min (A)	N_2/H_2	77.19	0.86	6.04	14.29	366
750°C 30 min (A)	N_2/H_2	78.40	1.49	13.43	29.25	210
750°C 30 min (B)	Ar	75.31	1.23	7.60	17.08	319
800°C 30 min (B)	Ar	83.88	0,8	8.83	18.55	278

Table 9 Optomechanical characteristics of the alloy (2) after being solubilised at various temperatures.

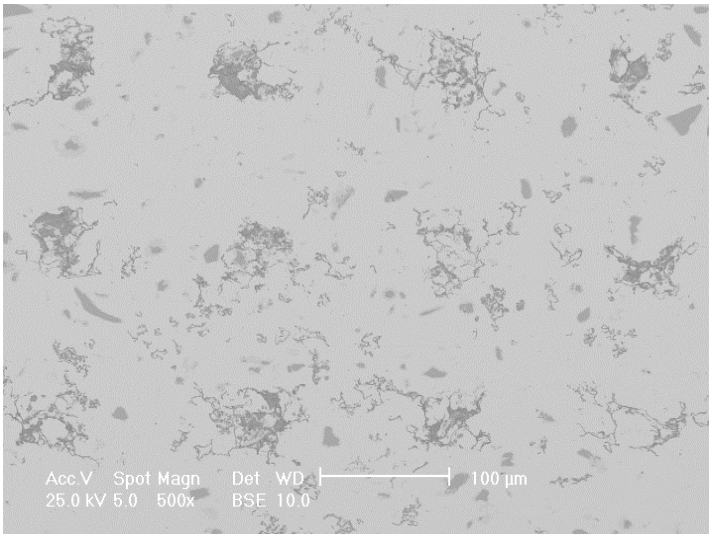

Figure 31 Electron microscopy of the alloy (2) after being solubilised at 750°C for 30 minutes (Ar).

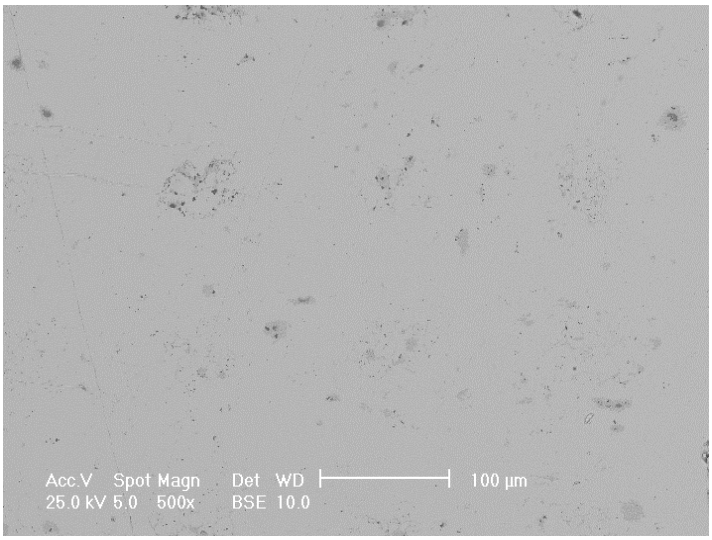

Figure 32 Electron microscopy of the alloy (2) after being solubilised at 800°C for 30 minutes (Ar).

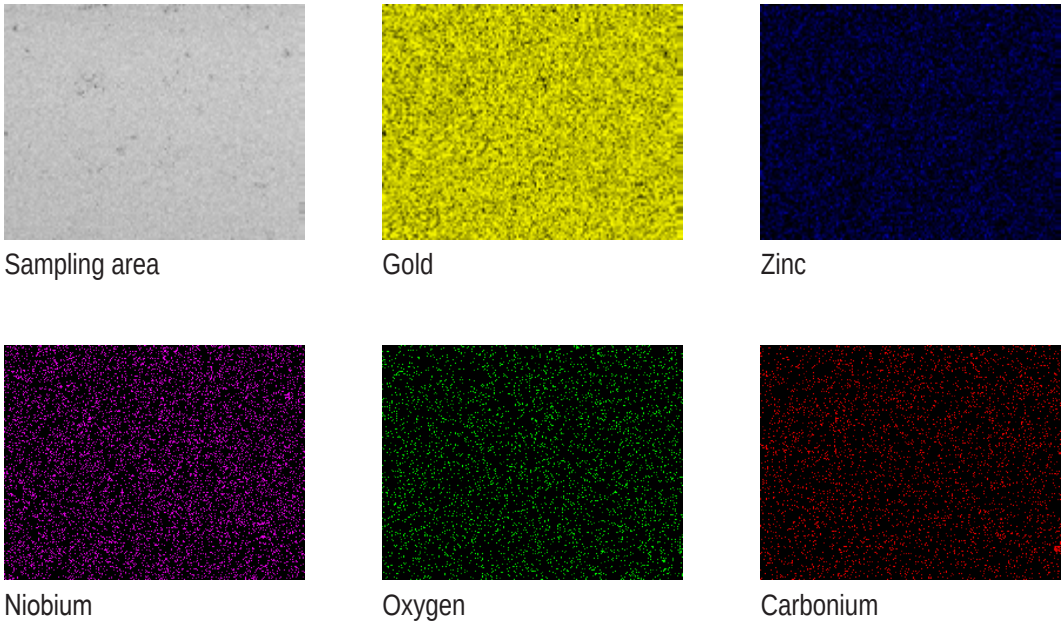

Figure 33 Map of the elements for the alloy (2) after being solubilised at 800°C (Ar).

To build a solid ring we chose the combination of parameters (A) with power of 37.5 W, a speed of 0.25 m/s and a hatch distance of 130 µm. Once polished, the rings created are white in colour (Figures 34, 35). However, polish on the reference wedding ring just printed shows a certain satiny finish due to the heterogeneous stages rich in niobium, though very uniform. We obtained a reduction in the satiny surface finish of this type of ring with thermic solubilisation treatment, which, however, enhanced the shine (Figure 36).

Figure 34 Solid ring printed with alloy (2) and power of 37.5 W (A).

Figure 35 Solid ring of the alloy (2) just printed after polishing.

Figure 36 Solid ring of the alloy (2) after solubilisation and polishing.

The last alloy with refractory metals used in selective laser melting contains titanium and silver as an ausiliary element, replacing zinc. The atomised matrix is 90%p gold and 10%p silver, added to the titanium powder so that the final consideration of this refractory element is 16.4%p and the gold one 750‰ of the alloy (3).
The morphology (Figure 37) and granulometric distribution of the binary pre-alloy gold silver (Figure 39) are consistent with the first matrix (Au-Zn), even if fashion is centred on slightly bigger size values (30 µm). The mixture of the precious matrix powder and titanium is much more uniform than in previous cases, as the refractory metal particles are round in shape and the same size as the matrix (Figure 39).
Unlike niobium (Tm = 2477°C, r = 152 nW·m), the titanium tends to solubilise much better in selective laser melting, probably because of its decidedly lower melting temperature and electric resistivity about three times greater (Tm = 1668°C, r = 420 nW·m), meaning more effective absorption of the laser radiation. Therefore, the items' micro-structure shows a lesser presence of titanium particle inclusions even at the rough, just printed state. In this case, the material printed is much more like a true solution at the solid state than a metallic matrix composite, as the quantity of strengthening particles in pure titanium can be really small, based on the laser parameters used.

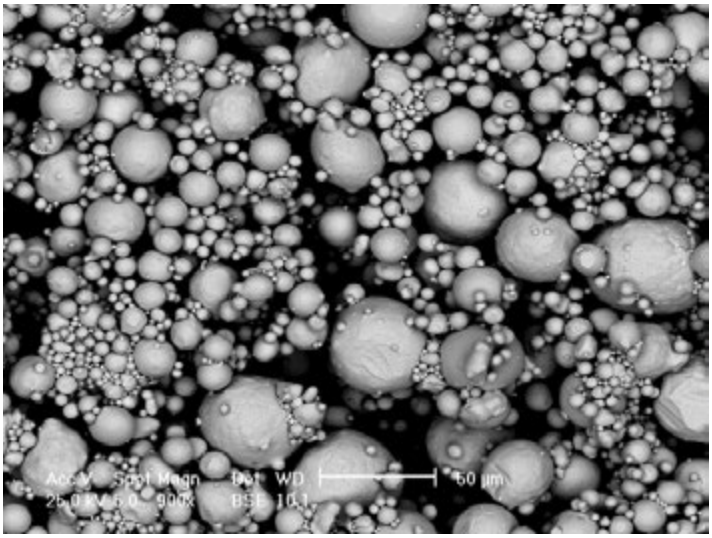

Figure 37 Scanning electron microscopy of the gold silver matrix.

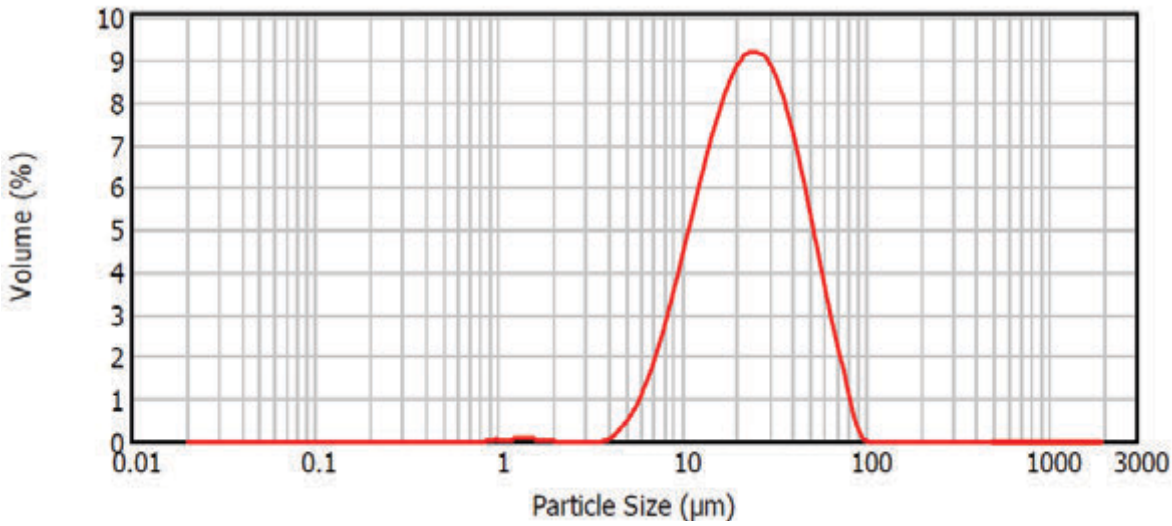

Figure 38 Granulometric distribution of gold silver matrix.

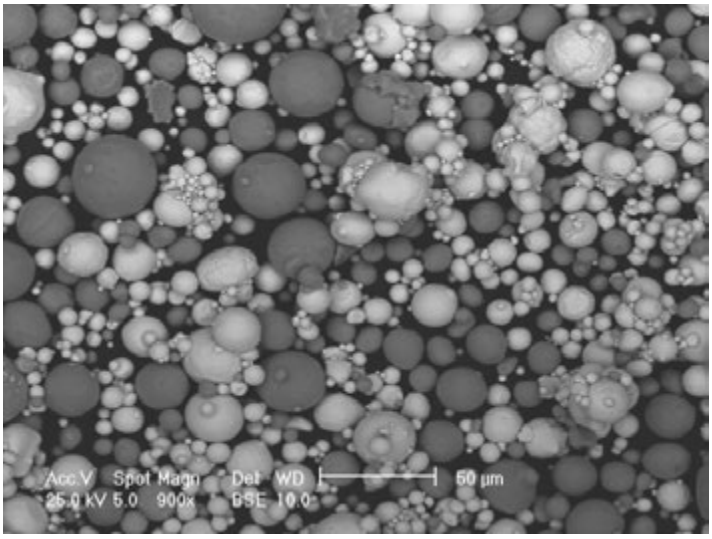

Figure 39 Scanning electron microscopy of the mixture of powders for the alloy (3).

The preliminary melting of the vectors and the solid prisms highlighted a fairly singular aspect with the gold powders containing high titanium concentrations. The laser radiation in the contact point with the powder produces a considerable scattering of melted lapilli, going to dirty the other growing zones of the pieces. Despite this, the best of the lamellar models used to control quality of the linear melting of the single vectors show good material rib continuity (Figure 40), though the vectors' profile is rather corrugated. The single vectors appear to be made of irregular portions of variable composition materials, due to partial homogenisation of the titanium with the precious matrix.

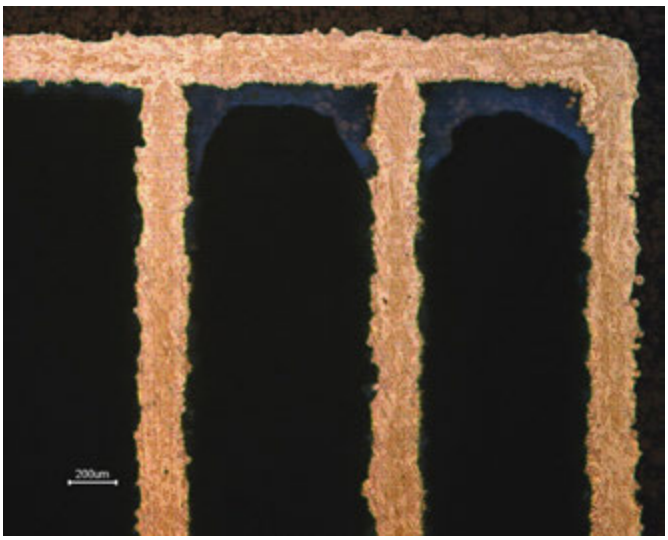

Figure 40 Metallographic section of a lamellar model (A).

In the case of solid models, the lapilli phenomenon forced us to limit the laser power to 50 W or to use a numerous scanning mode (XXX), starting with a first scan at very low power (20 W) and continuing with two much more energetic ones. In the same way as the previous cases, a group of four laser combinations was chosen for the titanium alloy (3), to get better metal solubilisation conditions and micro-structural integrity. The hatch distance was kept constant at 150 µm, as was the scanning speed; which, however, springs from different values differing in exposure time and distance of laser impulses (Table 10 and 11). The scanning methods adopted are XX and XXX.

ALLOY	SAMPLE	LASER POWER w	SCANNING SPEED (m/s)	DISTANCE VECTORS (µm)	SCANNING
3	A	50	0.25	150	XX
	B	20 - 75 - 50	0.25	150	XXX
	C	20 - 62.5 - 45	0.25	150	XXX
	D	50	0.25	150	XX

Table 10 Best laser parameter combinations for the selective melting of Au-Ti-Ag 750‰ (3

ALLOY	SAMPLE	L*	a*	b*	Y.I.	Rtot (µm)	HARDNESS (HV)
3	A	78.85	0.67	5.98	13.72	53	274
	B	78.80	0.55	5.50	13.22	54	288
	C	78.83	0.74	5.59	12.60	61	293
	D	78.78	0.70	6.50	14.83	56	279

Table 11 Optomechanical characteristics in function of laser parameters for the alloy (3).

The hardness measured on these samples can reach values close to 300 HV so be significantly higher than a classic white gold alloy 750‰ with a concentration similar to nickel equal to 12%p (240 HV), in the just melted conditions (Table 11). Moreover, the yellow indicator can drop to exceptionally low values (Y.I. D1925 = 12.60), lower than pure palladium (Y.I. D1925 = 13.63).
The metallographic analysis of the solid prisms built with the best parameters (Table 10) generally revealed presence of a good lateral junction of the vectors, with discrete porosity mainly localised on the vector and rare light and dark band zones following the trend of the laser scans, indicating local dishomogeneousness in the titanium concentration (Figure 41). The average porosity detected from digital analysis of the metalligraphic sections was comparable for all the samples, with an average value of 0.22±0.04% of the area analysed. In the case of sample (D) (Figure 42) we also detected a considerable presence of cracks, mainly of the inter-vectorial type. But with some cutting the vector perpendicularly. This provision suggests that cracks forming depends on the thermal tensions developed during printing, and not on an incomplete lateral junction of vectors due to imperfect printing parameters. This could indicate limited, intrinsic material ductility due to its composition. In fact, even if the titanium concentration was chosen to take the alloy system as close as possible to the stability region of the stage gAuTi (Figure 24), which has a certain ductility [9], the presence of silver as auxiliary metal could be responsible for the reduction in alloy plasticity through formation of intermetallics (AgTi2) with the titanium.

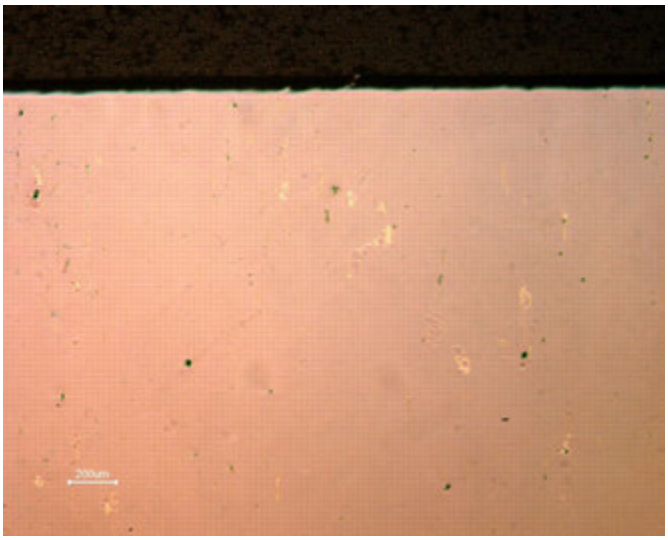

Figure 41 Example of metallographic section of the solid prisms in alloy AuAgTi (B).

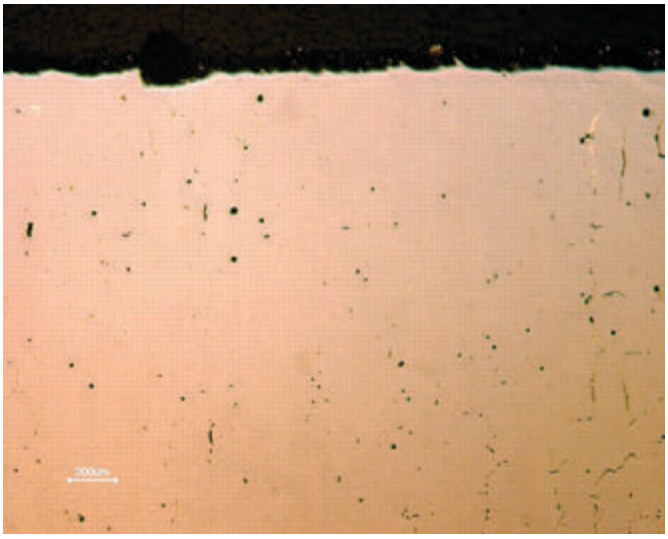

Figure 42 Metallographic section of the solid prism (D), with evident cracks.

The same prisms observed under the electronic microscope confimed what was established by the metallographic analyses, highlighting the presence of particles trapped in the matrix, in particular in sample (A) (Figure 43). One of these particles is enlarged in Figure 45. EDX microanalysis confirms a composition of just about pure titanium in the centre of the particle (Figure 45) and a transition halo with immediate composition between particle and matrix. In the case of samples printed with parameters B, C and D, the presence of titanium particles is much more reduced (Figure 46). In all the electronic images we can see a surface layer of a few tens of micrometers with numerous undissolved titanium particles simply incorporated in the precious matrix.

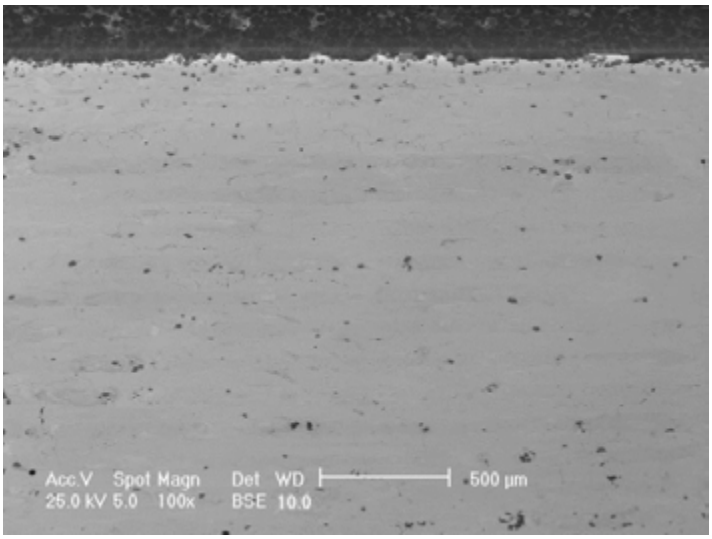

Figure 43 Electron microscopy of the solid prism (A).

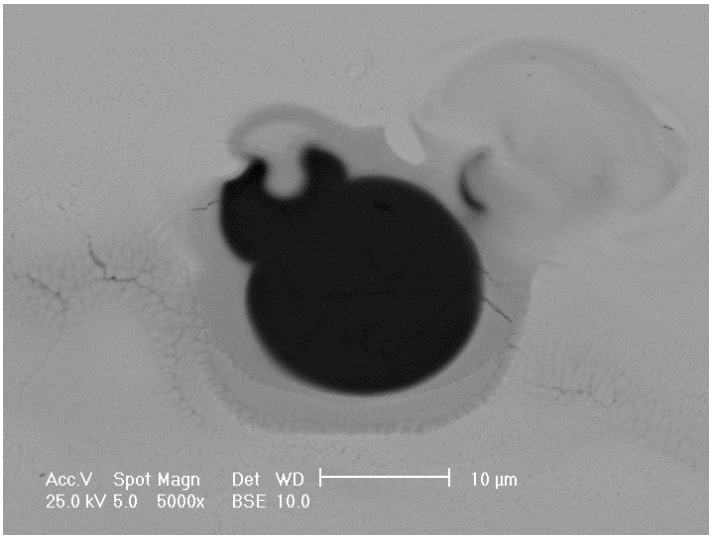

Figure 44 Electron microscopy of one of the titanium particles.

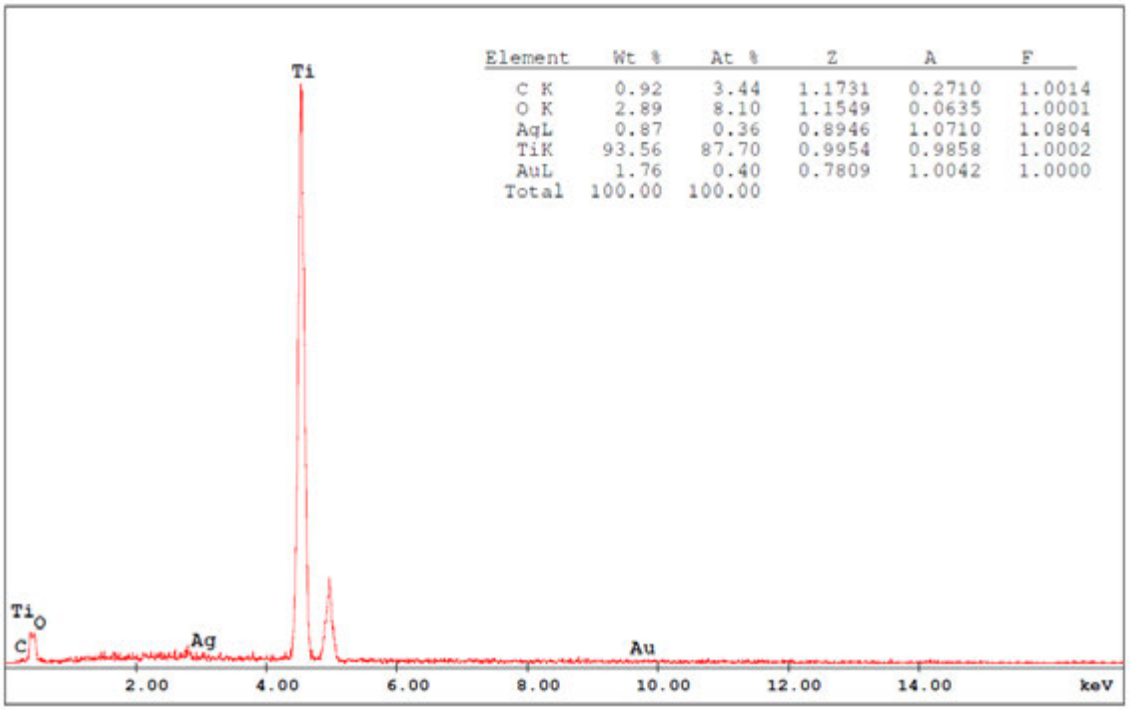

Figure 45 Microanalysis (EDX) of the titanium particle included in the metallic mass (A).

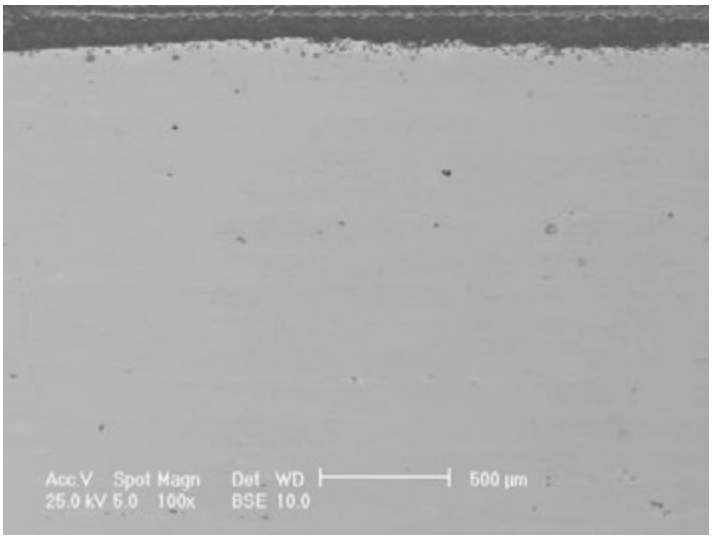

Figure 46 Typical electron microscopy of prisms B, C and D.

Confirmation of the just about complete solubilisation of the titanium can also be found in the map of the elements on a polished section of the solid prism (Figure 47). The titanium appears to be dispersed fairly uniformly, though you can see an unaltered particle and a porosity. The oxygen present does not seem to be concentrated in the refractory particles, but unifomly spread in the material; this means that printing conditions are characterised by a sufficiently low oxygen concentration to avoid the titanium oxidation.

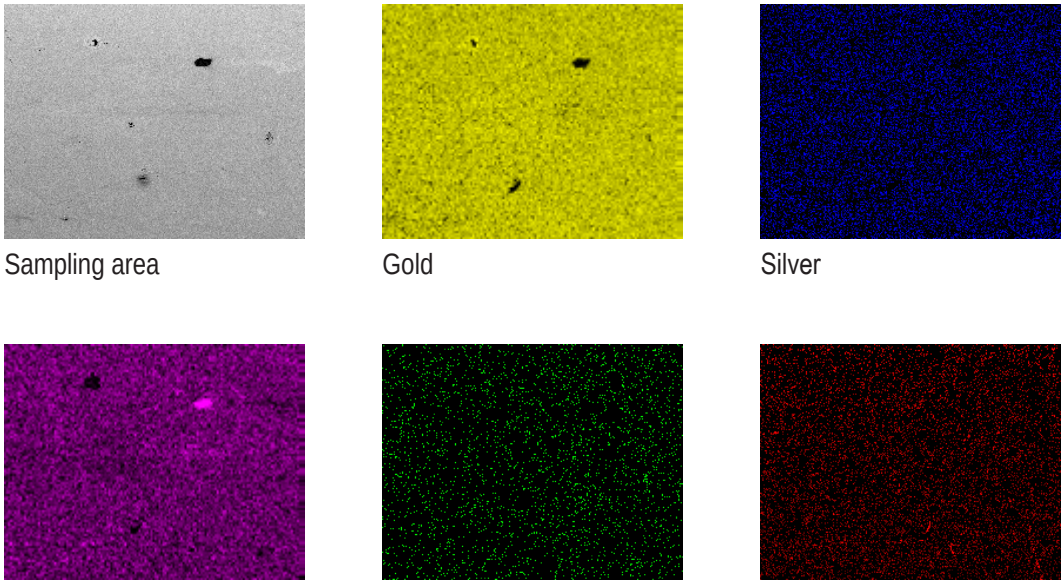

Figure 47 Map of the elements for the alloy (3) after printing.

Thanks to the almost total solubilisation of the titanium following simple printing, the yellow index values for the alloy (3) can drop to lower values than those observed for the niobium alloy(2) before solubilisation.
The metallographic attack of a horizontal section of the solid prism reveals the presence of a fairly homogeneopus, long range microstructure; however, at local level there are evident stage concentration zones (Figure 48). The metallographic examination highlights traces of the laser passage and a certain degree of inter-mixing of vectors, favouring piece consolidation. The granular structure can only be appreciated in some small, strongly enlarged areas (500X, Figures 48 and 49) highlighting a crystals dimension around 10 µm, as the solidification kinetics and localisation of the melted area do not allow for the growth of grains visible though the optic metallographic microscope.
Like niobium, the golden concentration of the titanium alloys measured using the same analytical techniques highlighted a very similar overall variation interval, between about 700‰ and 780‰ in gold. This strong resemblance leads us to believe that the phenomenon of gold concentration heterogeneity cannot just be attributed to the shape of the particles, irregular for niobium and spheric for titanium, but to the possible sedimentation of the precious particles on the work table, which can occur in both situations.

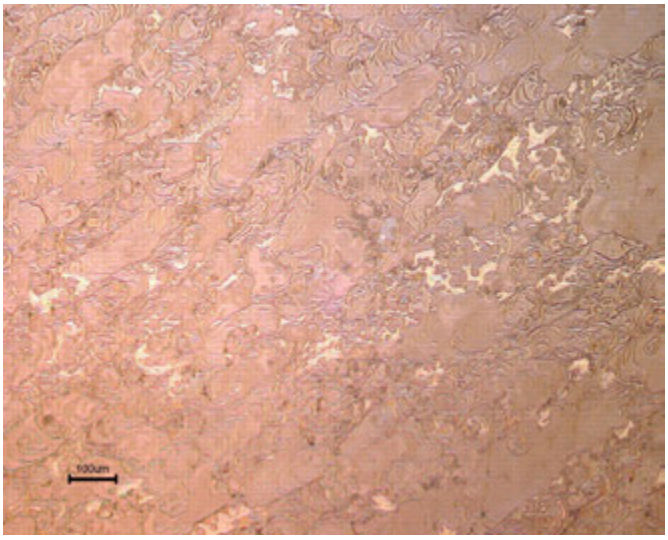

Figure 48 Metallographic section after chemical attack (100X) of the solid sample (A).

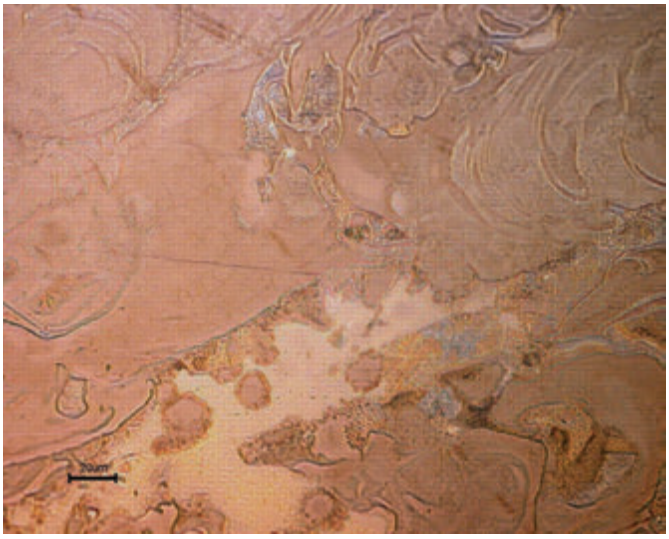

Figure 49 Metallographic section after chemical attack (500X) of the solid sample (A).

Despite the fact that with titanium the starting micro-structure is much more homogeneous than with niobium, some thermic solubilisation treatments wer performed on solid prisms to promote full material homogenisation. However, results were not satisfactory. The reduction in hardness and increase in the yellow indicator compared to the condition just printed (Table 12) indicate conduct that is the contrary to what usually occurs with niobium.
The solubilisation treatment at 900°C for 30 minutes displays a basic tendency of titanium particles to remain confined and unaltered in the initial particles, as indicated by the electronic micrographies performed in the same previous positions (Figures 50 and 51). On the other hand, following this thermic treatment we can see a discrete increase in cracks and slight increase in the spread of the titanium towards the matrix, visible from the thickening of the dark grey crown around the same pure titanium particle (Figures 44 and 54).

TEMPERATURE:	GAS	L*	a*	b*	Y.I. (D1925)	HARDNESS (HV)
after printing (C)	Ar	78.83	0.74	5.59	12.60	293
900°C 30 min	Ar	79.20	0.67	6.43	14.37	271
1100°C 30 min	Ar	78.66	1.07	6.49	15.02	274

Table 12 Optomechanical characteristics of the alloy (5) after being solubilised at various temperatures.

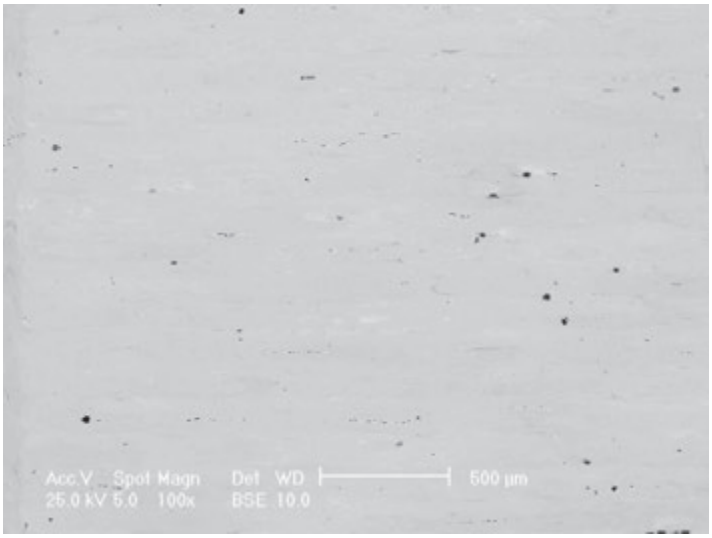

Figure 50 Scanning electron microscopy (100x) of the alloy (5) after the laser printing (C).

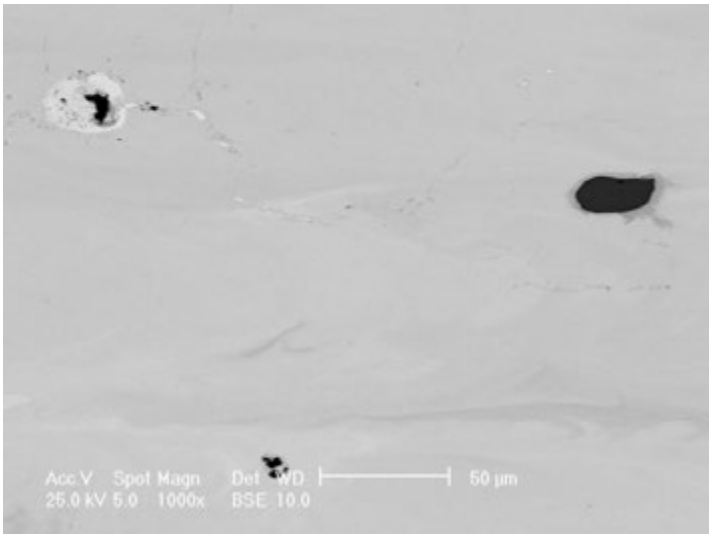

Figure 51 Scanning electron microscopy (1000x) of the alloy (5) after the laser printing (C).

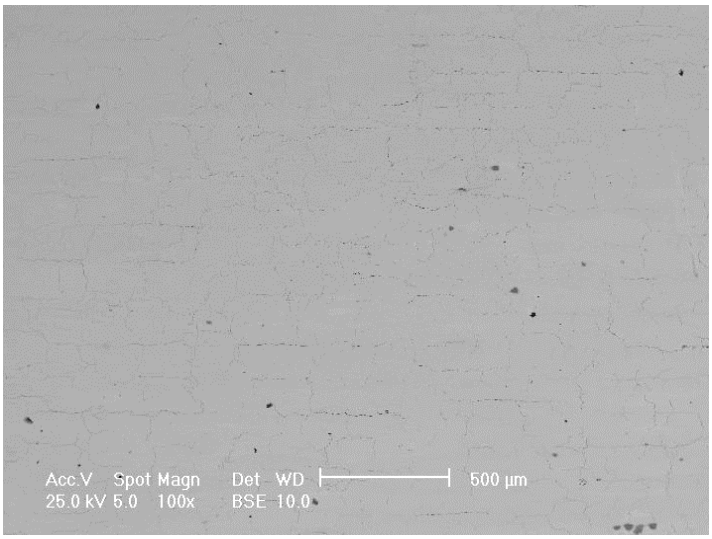

Figure 52 Scanning electron microscopy (100x) of the alloy (5) after solubilisation at 900°C

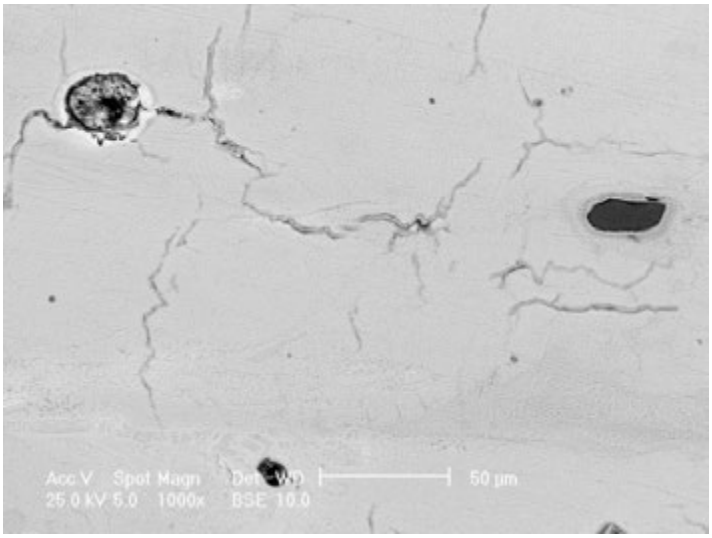

Figure 53 Scanning electron microscopy (1000x) of the alloy (5) after solubilisation at 900°C

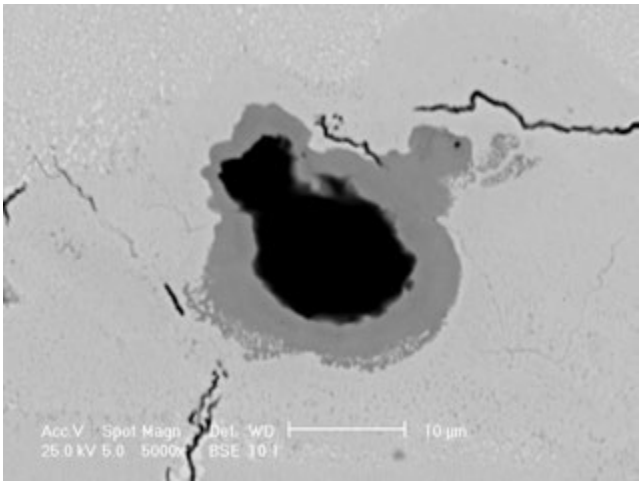

Figure 54 Scanning electron microscopy (5000x) of the alloy (5) after solubilisation at 900°C

Cracks forming is another factor tending to increase based on the solubilisation temperature. The treatment at 1100°C has considerably increased cracks and the spread of titanium, tending to react with the silver in proximity of its original particles (Figures 55 and 56).
The dark grey halos (Figure 54) around cracks are, in fact, formed by a relatively high percentage of silver compared to the alloy's nominal value (5). Solubilisation at a higher temperature managed to cause almost complete reabsorption of the titanium particles by the matrix. In fact, the dark dotting visible in the electron microscopy in Figure 55 is only porosity, even though it has also caused the proximal reaction with silver.

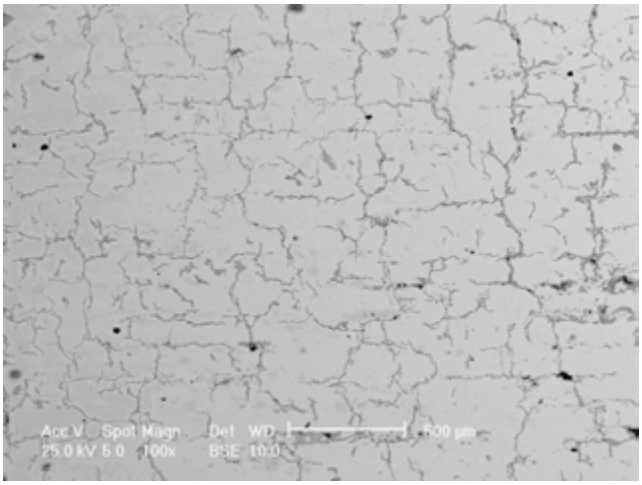

Figure 55 Scanning electron microscopy (100x) of the alloy (5) after solubilisation at 1100°C

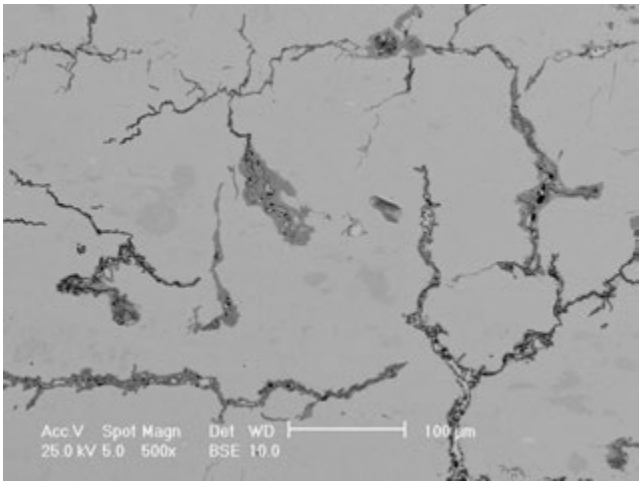

Figure 56 Scanning electron microscopy (500x) of the alloy (5) after solubilisation at 1100°C

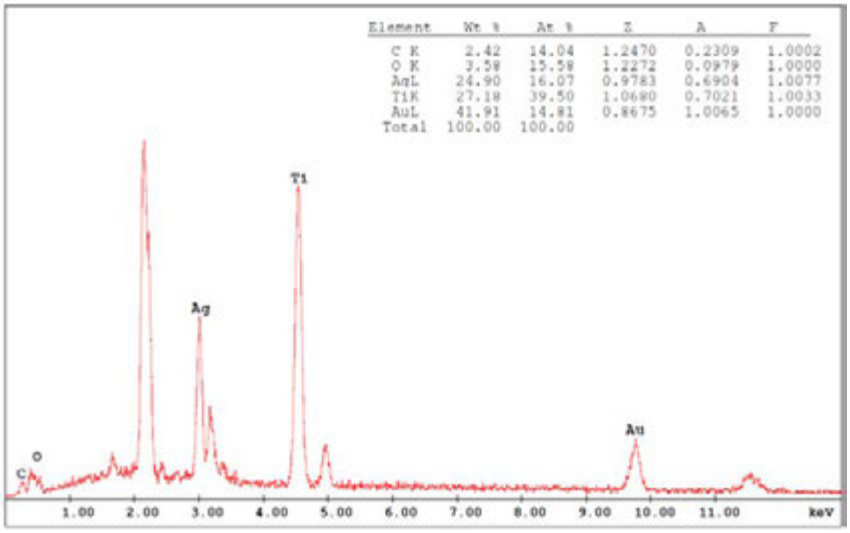

Figure 57 Microanalysis (EDX) of the titanium particle included in the metallic mass (A).

Confirmation of this silver and titanium concentration in proximity of the cracks can also be seen from the map of elements after solubilisation at 1100°C (Figure 58). Ratios between atomic particles probably indicate the formation of the inter-metallic Ti2Ag, which can constitute the material's least ductile element so be seat of the easier formation of cracks.

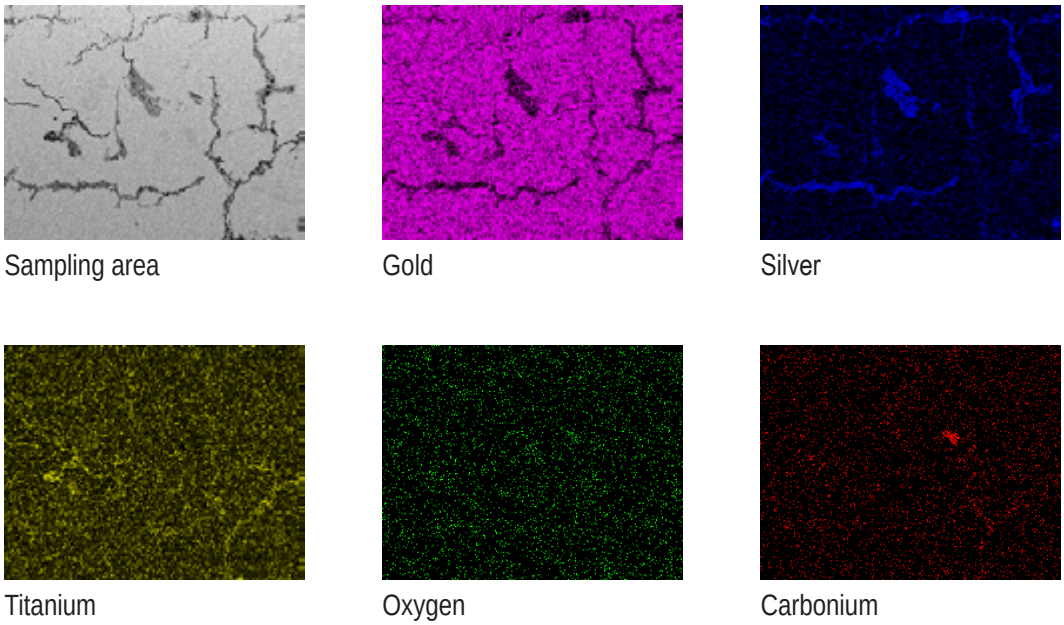

Figure 58 Map of the elements for the alloy (5) after solubilisation at 1100°C.

Following the metalographic results, the control ring was printed with a multiple scanning mode (XXX) in order to reduce porosity (B). Complete reabsorbtion of the refractory metal particles by the precious matrix is preferable, as, in the finishing stage, the surfaces take on a shiny, more brilliant look; though this can be considered a natural defect as in the definition of composite material the presence of stages extraneous to the matrix is implicit.
The yellow colour of the ring just printed (Figure 59) can be explained by the presence of a surface layer some tens of micrometers thick rich in undissolved titanium particles and simply immersed in the yellow colour precious matrix, similarly to what was observed in the solid prisms (Figures 43 and 46). As expected, the colour of the ring polished in white titanium gold is decidedly whiter than the ring in gold alloy with niobium (Figure 60) [10]. Density measurements performed on the rings produced confirmed a considerable characteristic expected for this alloy, the low density value. Values obtained are around 12.0 g·cm-3; that is about 18% less than the same classic alloy in nickel (about 14.6 g·cm-3) and even 25 % less than the equivalent alloy with palladium, whose density is about 16.0 g·cm-3. The possibility to have a legal concentration 750‰ (18 k) alloy in gold with a very low density enables us to reduce the weight of jewels, for the same volume.

The rings were subjected to anodizing treatment to check whether the extraordinary titanium colouring properties under electric tension can also be transferred to the precious alloy; thus create a material with innovative optic characteristics. However, a ring printed using a multiple scanning mode (B) and subjected to a classic industrial anodizing process (Figure 61) does not display interesting colouring. The amber green grading obtained is not uniform even if the shine of the original polished piece is partly preserved. The resulting colour could partly depend on dilution of the titanium in the gold matrix, which does not permit formation of coloured titanium oxide film; but also on other factors due to the high electric tension applied (30-150V) which could lead to the gold oxidising, and surely requires further analysis.

Figure 59 Solid ring (B) printed with alloy (3).

Figure 60 Solid ring of the alloy (3) just printed after polishing.

Figure 61 Ring (B) before and after industrial anodizing treatment.

CONCLUSIONS

Selective laser melting (SLM™) has shown considerable potential in the manufacture of jewellery created with innovative materials. Amorphous metals can preserve a considerable fraction of their glassy stage after the laser printing process; so continue to display their surprising mechanical performance, such as high level of hardness and resistance. The surface and internal quality of articles are still rough and porous, but considering the novelty of their debut with the selective laser melting technique, the result can be deemed worth mentioning. Selective laser melting has also proved it is possible to attach precious metals to refractory metals, creating very hard, white alloys, where manufacture would be truly difficult with a traditional system. Niobium, for example, was first incorporated uniformly in a precious gold and zinc matrix by selective laser melting. Then the refractory metal was homogenised through a solubilising thermic treatment, to obtain items that can reach 320 HV and a gold indicator (D1925) of 17.08. The titanium was introduced in alloy (16.4%p) using a gold and silver matrix completely similar to niobium, providing exceptional yellow indicator (12.60) values and hardnesses that were almost just as high, combined with considerably reduced density, lesser by about a quarter than an equivalent alloy with palladium and equal to 18% less compared to a classic white gold alloy with nickel. The total of residual defects observed in samples produced is, above all, of a micro-structural kind and includes micro, inter and trans-vectorial cracks, porosity from partial melting of the metallic powder and, secondly, widespread residues of particles of pure refractory metals that had not dissolved in the matrix which, in the finishing stage, can reduce the shine of the alloy in favour of a satiny surface.

BIBLIOGRAPHY

SFS Papers
[1] D. Zito et al., “Latest developments in Selective Laser Melting production of gold jewellery”, The Santa Fe Symposium on Jewelry Manufacturing Technology 2012, ed. Eddie Bell (Albuquerque: Met-Chem Research, 2012).
[2] D. Zito et al., “Optimisation of the Main Selective Laser Melting Technology Parameters in the Production of Gold Jewellery”, The Santa Fe Symposium on Jewelry Manufacturing Technology 2013, ed. Eddie Bell (Albuquerque: Met-Chem Research, 2013).
[3] D. Zito et al., “Optimization of SLM Technology Main Parameters in the Production of Gold and Platinum Jewelry”, The Santa Fe Symposium on Jewelry Manufacturing Technology 2014, ed. Eddie Bell (Albuquerque: Met-Chem Research, 2014).
[4] D. Zito et al., “Definition and solidity of gold and platinum jewels produced using Selective Laser Melting SLM™ technology”, The Santa Fe Symposium on Jewelry Manufacturing Technology 2015, ed. Eddie Bell (Albuquerque: Met-Chem Research, 2015).
[5] B. Lohwongwatana, J. Schroers, W. L. Johnson, “Liquidmetal – Hard 18K and 850 Pt Alloys That Can Be Processed Like Plastics or Blown Like Glass”, The Santa Fe Symposium on Jewelry Manufacturing Technology 2015, ed. Eddie Bell (Albuquerque: Met-Chem Research, 2015).
6. E. Klotz, M. Eisenbart, “Gold based solid metallic glasses - hard like steel, moldable like plastics”, The Santa Fe Symposium on Jewelry Manufacturing Technology 2013, ed. Eddie Bell (Albuquerque: Met-Chem Research, 2013).
7. E. Klotz, T. Heiss, “Investment Casting of titanium alloys by induction melting”, The Santa Fe Symposium on Jewelry Manufacturing Technology 2015, ed. Eddie Bell (Albuquerque: Met-Chem Research, 2015).
Article journals
[8] J. Schroers, B. Lohwongwatana, W. L. Johnson, A. Peker, “Gold based solid metallic glass”, Applied Physics Letters 87, 061912 (2005).
[9] Hyunbo Shim, Masaki Tahara, Tomonari Inamura, Kenji Goto, Yoko Yamabe-Mitarai, Hideki Hosoda, “Oxidation Behavior of Au-55 mol%Ti High Temperature Shape Memory Alloy during Heating in Ar-50 vol%O2 Environment” Materials Transactions, Vol. 56. 4 2015 6735794600 344 604
[10] S. Henderson, D. Manchanda, “White Gold Alloys: Colour Measurement and Grading” Gold Bulletin 2005, 38/2.